Int J Fract (2018) 210:113–136
https://doi.org/10.1007/s10704-018-0265-z

ORIGINAL PAPER

Achieving pervasive fracture and fragmentation in three-dimensions: an unstructuring-based approach

Daniel W. Spring · Glaucio H. Paulino

Received: 19 August 2017 / Accepted: 23 January 2018 / Published online: 3 February 2018

Abstract There are few methods capable of capturing the full spectrum of pervasive fracture behavior in three-dimensions. Throughout pervasive fracture simulations, many cracks initiate, propagate, branch and coalesce simultaneously. Because of the cohesive element method framework, this behavior can be captured in a regularized manner. However, since the cohesive element method is only able to propagate cracks along element facets, a poorly designed discretization of the problem domain may introduce artifacts into the simulated results. To reduce the influence of the discretization, geometrically and constitutively unstructured means can be used. In this paper, we present and investigate the use of three-dimensional nodal perturbation to introduce geometric randomness into a finite element mesh. We also discuss the use of statistical methods for introducing randomness in heterogeneous constitutive relations. The geometrically unstructured method of nodal perturbation is then combined with a random heterogeneous constitutive relation in three numerical examples. The examples are chosen in order to represent some of the significant influencing factors on pervasive fracture and fragmentation; including surface features, loading conditions, and material gradation. Finally, some concluding remarks and potential extensions are discussed.

Keywords Pervasive fracture · Fragmentation · Nodal perturbation · Cohesive elements · Extrinsic PPR model · Weibull distribution

1 Introduction

The pervasive fracture and fragmentation of structures occurs at various scales and in various contexts. When a structure is struck with either a high-velocity direct impact or a blast load, the damage incurred typically pervades a region of the structure. Pervasive damage involves the entire spectrum of fracture behavior; from crack initiation, through crack propagation, branching and coalescence, all the way to complete fragmentation. At any one time, there may be hundreds or thousands of micro- to macro-cracks in the structure. Being able to model and understand the factors which influence the fragmentation of structures can lead to better design practices in many fields of engineering. For example, understanding how a ceramic plate fragments when struck with a high velocity projectile can improve the design of armor for personnel carriers. Alternatively, understanding the process by which a kidney stone fragments may help in the design of surgical tools and procedures. However, due to the inherent complex-

D. W. Spring
Department of Civil and Environmental Engineering, University of Illinois at Urbana-Champaign, Urbana, IL, USA
e-mail: spring2@illinois.edu

G. H. Paulino (✉)
School of Civil and Environmental Engineering, Georgia Institute of Technology, Atlanta, GA, USA
e-mail: paulino@gatech.edu

ity of modeling pervasive damage, there are few numerical methods capable of capturing the full spectrum of behavior in three-dimensions.

Currently, there are many methods which have been proposed for simulating fracture problems. Some of the popular methods consist of the extended (or generalized) finite element method (FEM); meshless or particle based methods; peridynamics (Silling and Bobaru 2005; Bažant et al. 2016), and the cohesive element method. The extended FEM uses discontinuous shape functions to represent the profile of a crack within a continuum. The discontinuity in the element's shape function effectively splits the element; which requires a lot of heuristic manipulations, and can present numerical integration and time-stepping issues in dynamic fracture simulations (Park et al. 2012). In three dimensions, the extended FEM has proven useful in modeling fracture problems dominated by a single crack (Sukumar et al. 2000; Areias and Belytschko 2005). However, when faced with the full spectrum of fracture behavior, the extended FEM can become prohibitively complicated (Bishop 2009).

Rather than using elements to discretize the problem domain, meshless methods represent the unknown fields with nodal information (Nguyen et al. 2008). By increasing the number of nodes dispersed in a region, a higher resolution of information in that region is obtained. Thus, nodes are typically clustered around the critical portions of the domain; which, in fracture problems, is the crack-tip. Each node is contained within a nodal-support region and a weight function is defined over each nodal-support region. The spacing of the nodes is such that each point in the domain is covered by at least three distinct weight functions. The resulting global fields are then interpolated from nodal information using a Moving Least Squares fitting procedure (Lancaster and Salkauskas 1981). Examples of meshless methods include the Diffuse Element Method (Nayroles et al. 1992), the Element Free Galerkin method (Belytschko et al. 1994a, b; Belytschko and Fleming 1999), the Reproducing Kernel Method (Liu et al. 1995), the Meshless Local Petrov–Galerkin method (Atluri and Zhu 1998), the cracked particles method (Rabczuk and Belytschko 2004), and the Material Point Method (Sulsky and Schreyer 2004). Although meshless methods have shown some promise in modeling problems where fracture is dominated by a single crack, many of them still suffer from volume deletion during pervasive fracture and fragmentation problems. As the continuum material fragments, it evolves into a collection of spheres; which have a theoretical maximum packing limit of 74% (Bishop 2009), leading to a nonphysical loss of volume in the model.

The cohesive element method, motivated by the work of Dugdale (1960) and Barenblatt (1959), uses cohesive zone models to explicitly represent the inelastic zone of damage in front of the crack tip. In dynamic fracture simulations, extrinsic cohesive elements are adaptively inserted ahead of a propagating crack tip and resist the separation of the adjacent bulk elements through cohesive forces (Ortiz and Pandolfi 1999; Zhang et al. 2007). The insertion of cohesive elements is restricted to element facets. This restriction allows the cohesive element method some unique capabilities. The mesh topology regularizes the domain and naturally handles the branching and coalescence of fracture surfaces. The elements are not split, thus the minimum facet size is fixed, and time-stepping issues related to small facet sizes do not occur. Additionally, the restriction of fracture surfaces to element facets results in a continuous volume of bulk material as it fragments. However, restricting fracture to occur along element facets can result in mesh dependent behavior, and thus the mesh discretization in dynamic cohesive fracture simulations is important. If one were to choose a structured mesh, or to use mesh smoothing techniques on a randomly generated mesh, the resulting discretization could bias the fracture patterns. Thus, it is worth exploring means of introducing randomness into the problem.

Randomness can be introduced to a finite element problem through either topological, geometric, or constitutive means. The primary topologically unstructured methods consist of: remeshing, element splitting and adaptive refinement. With remeshing or adaptive refinement, the internal state variables of the fine mesh need to be interpolated from those of the coarse mesh. For refinement around a propagating crack tip, the repeated application of mesh-to-mesh transfer operators may result in significant numerical diffusion (Mosler and Ortiz 2009). Additionally, these methods are not particularly suitable to pervasive fracture problems, as the entire domain often needs to be refined, quickly losing the cost-saving advantages of adaptive refinement. Alternatively, some researchers apply element splitting techniques to increase the number of crack paths in three-dimensional tetrahedral meshes. The advantage of element splitting is that it may be combined with an edge-collapse operator

(Kallinderis and Vijayant 1993; Molinari and Ortiz 2002), to coarsen regions far from the crack tip. The downside of this technique is that edge-splitting only provides a small amount of refinement, and the quality of the elements can deteriorate once split.

In this paper, we present a combined geometric and constitutive approach for introducing randomness into otherwise structured numerical models, and apply it to the investigation of pervasive fracture and fragmentation behavior. First, a nodal perturbation technique is presented to alleviate the structure in meshes generated using automatic mesh generators. A study on the effect of the nodal perturbation is presented, where the metrics of Lo's parameter and maximum and minimum interior angles are used to quantify the effect of various nodal perturbation factors on mesh quality. As a result of the study on mesh quality, a maximum value for the nodal perturbation factor is recommended and is used throughout the remainder of the paper. Additionally, a Weibull distribution is motivated as a means of generating a random heterogeneous constitutive relation. The combined effect of the geometrically random (via nodal perturbation) and constitutively random (via a random assignment of material strength) methods is investigated in a series of examples. The remainder of the paper is organized as follows. Section 2 outlines the numerical framework for our study. The cohesive zone model selected to represent the dynamic failure behavior is the extrinsic Park–Paulino–Roesler (PPR) model. An overview of the model is presented in Sect. 3, along with a discussion on using random heterogeneous constitutive relations for introducing randomness into a model. Section 4 outlines the technique of nodal perturbation, to introduce geometric unstructuredness into a finite element mesh. Additionally, in this section, we outline the series of geometric studies used to investigate the influence of nodal perturbation on the quality of the mesh. In Sect. 5 we present three numerical examples which highlight many of the significant factors influencing the pervasive fracture and fragmentation of structures. Finally, we provide some concluding remarks in Sect. 6.

2 Numerical framework

In this work we use cohesive elements, within the finite element framework, to model fracture. There are two classes of cohesive elements. *Intrinsic* cohesive elements are inserted to the model prior to the simulation (Zhang and Paulino 2005) and are convenient when fracture is restricted to occur along a specified line or in a specified region. However, this approach is known to alter the effective properties of the bulk material in the zone of fracture (Falk et al. 2001; Klein et al. 2000). Alternatively, *extrinsic* cohesive elements can be inserted to the mesh on the fly, where and when needed. Extrinsic elements are convenient for simulating problems where the location of fracture is not known a priori. The dynamic mesh connectivity, necessary for the adaptive insertion of extrinsic cohesive elements between bulk elements, is handled through a topological data structure (Celes et al. 2005; Paulino et al. 2008). The constitutive relation of the cohesive elements corresponds to the chosen cohesive model, as will be discussed in the next Section.

In fracture simulations it is important to take into consideration the effect of finite deformations. When cohesive elements are first activated, they display zero thickness, but as fracture progresses the adjacent bulk elements separate and rotate. By not taking into consideration these finite rotations the mechanics of the problem may not be accurately captured. In this work finite deformations are taken into account by means of the total Lagrangian formulation. In this formulation, the deformation is described with respect to the undeformed configuration. The expression of the principal of virtual work with respect to the undeformed configuration relates the sum of the virtual strain energy and virtual kinetic energy to the sum of the virtual work done by external and cohesive tractions:

$$\int_{\Omega} (\mathbf{S} : \delta\mathbf{E} + \rho\ddot{\mathbf{u}} \cdot \delta\mathbf{u})\, d\Omega = \int_{\Gamma_{coh}} \mathbf{T}_{coh} \cdot \delta\Delta\mathbf{u} d\Gamma_{coh} + \int_{\Gamma_{ext}} \mathbf{T}_{ext} \cdot \delta\mathbf{u} d\Gamma_{ext}, \quad (1)$$

where Ω is the domain in the reference configuration, $\mathbf{S} = J\mathbf{F}^{-1}\boldsymbol{\sigma}\mathbf{F}^{-\mathrm{T}}$ is the second Piola-Kirchoff stress tensor, $\mathbf{E}$ is the Green-Lagrange strain tensor, ρ is the material density, $\mathbf{u}$ is the displacement vector, $\ddot{\mathbf{u}}$ is the acceleration vector, $\mathbf{T}_{ext}$ is the traction applied along the external surface, Γ_{ext}, in the reference configuration, $\mathbf{F}$ is the deformation gradient, $J = \det\mathbf{F}$ is the Jacobian, and the internal displacement jump, $\Delta\mathbf{u}$, produces a cohesive traction, $\mathbf{T}_{coh}$, over the internal cohesive surface Γ_{coh} in the reference configuration. For implementation, Eq. (1) is expressed in matrix notation as:

$$\mathbf{Ku} + \mathbf{M\ddot{u}} - \mathbf{R}_{coh} - \mathbf{R}_{ext} = 0. \tag{2}$$

where $\mathbf{K}$ is the stiffness matrix, $\mathbf{M}$ is the mass matrix, $\mathbf{R}_{coh}$ is the cohesive force vector, and $\mathbf{R}_{ext}$ is the external force vector.

Numerically, to progress the dynamic simulation, time is discretized using the explicit central difference method (Newmark 1959). The computation of nodal displacements, velocities and accelerations at time $n+1$ are computed from those at time n through the following scheme:

$$\mathbf{u}_{n+1} = \mathbf{u}_n + \Delta t \dot{\mathbf{u}}_n + \frac{1}{2}(\Delta t)^2 \ddot{\mathbf{u}}_n \tag{3}$$

$$\ddot{\mathbf{u}}_{n+1} = \mathbf{M}^{-1}\left(\mathbf{R}_{ext} - \mathbf{R}_{int_{n+1}} + \mathbf{R}_{coh_{n+1}}\right) \tag{4}$$

$$\dot{\mathbf{u}}_{n+1} = \dot{\mathbf{u}}_n + \frac{\Delta t}{2}(\ddot{\mathbf{u}}_n + \ddot{\mathbf{u}}_{n+1}) \tag{5}$$

where Δt denotes the time step. Note that $\mathbf{R}_{int}$ and $\mathbf{R}_{coh}$ are the internal and cohesive force vectors obtained from the separate contribution of the bulk and cohesive elements, respectively. To compute the mass matrix, $\mathbf{M}$, we apply a standard mass lumping technique in which the diagonal terms of the consistent mass matrix are scaled, preserving the total mass and resulting in a diagonal mass matrix (Hinton et al. 1976; Hughes 2000).

3 Random heterogeneous constitutive relation by means of statistical distribution

This section outlines the constitutive relation selected for the cohesive elements and discusses the use of random methods for capturing microscale heterogeneity.

3.1 Park–Paulino–Roesler cohesive model

In the dynamic simulations performed in this work, cracks are represented through the use of cohesive zone elements. As mentioned previously, we use the extrinsic cohesive element approach. In this approach, the criterion to insert the cohesive element is external to the formulation. A cohesive element is inserted once the averaged normal or tangential stress along a facet exceeds the normal or tangential cohesive strength of the material, respectively. Once the element is inserted, its behavior is governed by the traction-separation relation of the extrinsic Park–Paulino–Roesler (PPR) cohesive model (Park et al. 2009). The extended formulation of the model can be found in the principal publication; below, we just include a brief summary for completeness.

The PPR cohesive model is potential-based, meaning that the traction-separation relation is derived from a potential and the unloading/reloading relation and contact formulation are independent of the model. The potential is given as:

$$\begin{aligned}\Psi(\Delta_n, \Delta_t) &= \min(\phi_n, \phi_t) \\ &+ \left[\Gamma_n\left(1 - \frac{\Delta_n}{\delta_n}\right)^{\alpha} + \langle \phi_n - \phi_t \rangle\right] \\ &\left[\Gamma_t\left(1 - \frac{|\Delta_t|}{\delta_t}\right)^{\beta} + \langle \phi_t - \phi_n \rangle\right],\end{aligned} \tag{6}$$

where the Macaulay bracket $\langle \cdot \rangle$ is defined such that $\langle x \rangle = (|x| + x)/2$.

The normal, T_n, and tangential, T_t, tractions are determined by taking the derivative of the potential with respect to the normal opening, Δ_n, and tangential opening, Δ_t, respectively. Hence,

$$\begin{aligned}T_n(\Delta_n, \Delta_t) &= -\alpha \frac{\Gamma_n}{\delta_n}\left(1 - \frac{\Delta_n}{\delta_n}\right)^{\alpha-1} \\ &\left[\Gamma_t\left(1 - \frac{|\Delta_t|}{\delta_t}\right)^{\beta} + \langle \phi_t - \phi_n \rangle\right]\end{aligned} \tag{7}$$

$$\begin{aligned}T_t(\Delta_n, \Delta_t) &= -\beta \frac{\Gamma_t}{\delta_t}\left(1 - \frac{|\Delta_t|}{\delta_t}\right)^{\beta-1} \\ &\left[\Gamma_n\left(1 - \frac{\Delta_n}{\delta_n}\right)^{\alpha} + \langle \phi_n - \phi_t \rangle\right]\frac{\Delta_t}{|\Delta_t|}\end{aligned} \tag{8}$$

where ϕ_n and ϕ_t are the mode I and mode II fracture energies, and α and β are the mode I and mode II shape parameters. The energy constants Γ_n and Γ_t are defined as:

$$\begin{aligned}\Gamma_n &= (-\phi_n)^{\langle \phi_n - \phi_t \rangle/(\phi_n - \phi_t)}, \\ \Gamma_t &= (-\phi_t)^{\langle \phi_t - \phi_n \rangle/(\phi_t - \phi_n)}\end{aligned} \tag{9}$$

for different fracture energies ($\phi_n \neq \phi_t$), and as:

$$\Gamma_n = -\phi_n, \qquad \Gamma_t = 1 \tag{10}$$

if the fracture energies are the same for both mode I and mode II separation, ($\phi_n = \phi_t$). In total, there are six user inputs to the extrinsic PPR cohesive model: ϕ_n, ϕ_t, α, β, and the mode I and mode II cohesive strengths σ_{max} and τ_{max}, respectively. A set of sample traction-separations relations are illustrated in Fig. 1.

For this study, the unloading/reloading relation is coupled, meaning that the unloading in the normal

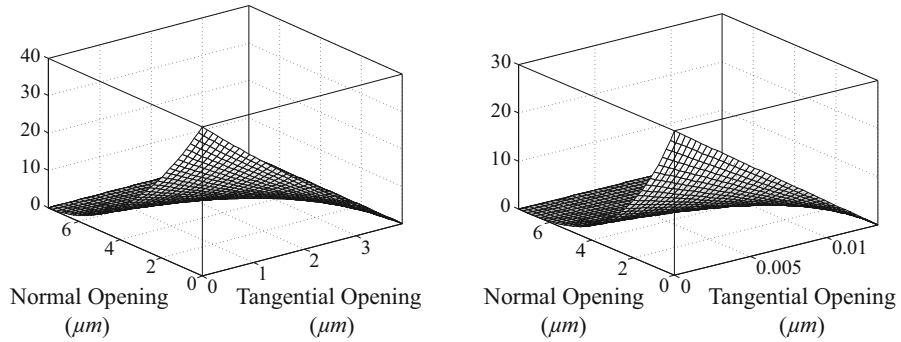

Fig. 1 Traction separation relations for **a** normal opening ($\phi_n = 100$ N/m, $\sigma_{max} = 40$ MPa, $\alpha = 3.0$), and **b** tangential opening ($\phi_t = 200$ N/m, $\tau_{max} = 30$ MPa, $\beta = 5.0$)

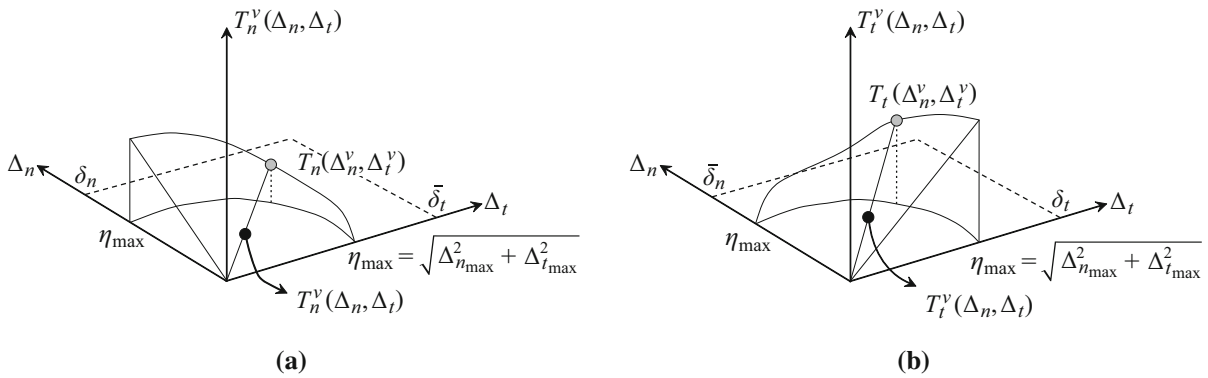

Fig. 2 Depiction of the coupled unloading schemes for **a** normal and **b** tangential interactions (Park 2009), with linear unloading/reloading to the origin

direction is coupled to that in the tangential direction. In addition, we assume that the unloading occurs linearly back to the origin, as seen in Fig. 2. Contact is assumed to occur when the normal separation within a cohesive element becomes negative. We use the penalty stiffness approach, in which a high stiffness counteracts the interpenetration of elements. This approach is popularly implemented in conjunction with cohesive elements, however, others are available (Simo et al. 1986; Espinosa et al. 2000; Falk et al. 2001; Spring et al. 2016).

3.2 Statistical methods for capturing material heterogeneity

While the focus of this work is on the investigation of homogeneous or homogenized materials, we recognize that all materials contain heterogeneity (or defects) at the microscale. Defects naturally arise in materials due to grain boundaries, voids, or inclusions (Becher et al. 1998; Sun et al. 1998). As well, defects can be introduced through the act of processing or machining the material (Levy 2010). These microscale defects constitute regions where stresses can concentrate and lead to damage or failure. In this work, the representation of this heterogeneity is achieved by means of a statistical distribution of material properties, specifically a distribution of the strength of the material.

Over the years, there have been many proposed models for capturing the distribution of defects in a material. One of the simplest models for incorporating defects in the material is to distribute the material parameters based on a constant probability density function (PDF); which is equivalent to a random perturbation to the material's properties (Ostoja-Starzewski and Wang 2006; Wang et al. 2008; Song and Belytschko 2009). While this model is simple, it has no physically motivated basis. Alternatively, one could take a statistical approach, distributing the material strength based on a probabilistic model (Bažant and Chen 1996). Peirce (1926) developed a probabilistic failure model based on

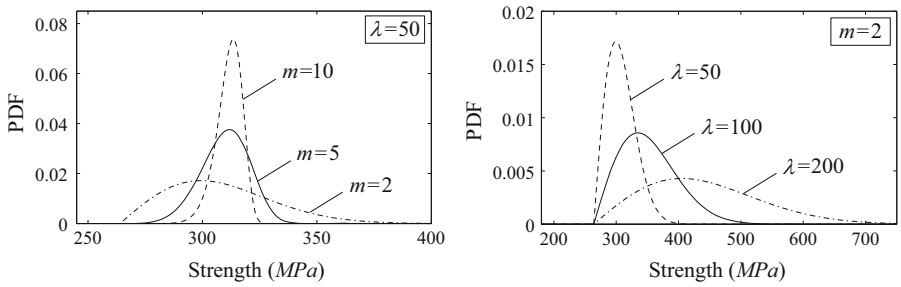

Fig. 3 Effect of input parameters on the Weibull distribution: **a** λ, and **b** m. Here we assume $\sigma_{min} = 264$ MPa and $V_0 = 1$

the weakest link theory and extreme value statistics. His model was later refined by Fréchet (1927), among others (Fischer and Tippett (1928) and von Mises (1936)). However, the most popular probabilistic model for the study of material failure is that of Weibull (1939).

Weibull's probabilistic failure model was motivated by randomness he observed in the ultimate failure strength of material specimens tested in an identical manner. He explained his motivation through a simple thought experiment. Consider a series of rods of length L, with cross-sectional area A, loaded to failure by an external load P. If one were to repeat this experiment the ultimate failure load would not be a constant, but would differ each time. The failure loads could then be grouped around a mean and a statistical analysis could be completed. Based on a set of experiments, conducted on a variety of materials with multiple loading conditions, he proposed the well known Weibull distribution with probability of failure P_f given by:

$$P_f = 1 - e^{-N(\sigma, V)} \tag{11}$$

where V is the volume of the material, σ is the measure of stress, and $N(\sigma, V)$ is a material function, independent of the position. The specific form of $N(\sigma, V)$ is often the topic of debate; however, Weibull noted that it must be a monotonically increasing function of σ and determined that an effective relation for most homogeneous materials is:

$$N(\sigma, V) = \frac{1}{V_0}\left(\frac{\sigma - \sigma_{min}}{\lambda}\right)^m \tag{12}$$

where m is the Weibull modulus, V_0 is a normalizing volume (often taken as $V_0 = 1$, Danzer 1992), λ is a scale parameter, and σ_{min} is the lower bound of material strength. To illustrate the influence of the Weibull modulus and scale parameter on the probability density function, some sample functions are illustrated in Fig. 3. The mean, median and variance of the Weibull distribution are calculated as

$$\sigma_{mean} = \sigma_{min} + \lambda\Gamma\left(1 + \frac{1}{m}\right), \tag{13}$$

$$\sigma_{median} = \sigma_{min} + \lambda \ln(2)^{\frac{1}{m}}, \tag{14}$$

$$Var(\sigma) = \lambda^2\left[\Gamma\left(1 + \frac{2}{m}\right) - \left(\Gamma\left(1 + \frac{1}{m}\right)\right)^2\right]. \tag{15}$$

In the years since Weibull presented his distribution, many researchers have proposed alternate forms of $N(\sigma, V)$. Freudenthal (1968) proposed a general distribution for homogeneous and brittle materials. He assumed that the flaws do not interact, and that the probability of failure only depends on the number of critical flaws, $N_{c,S}$, present in a specimen of size S:

$$N(\sigma, V) = N_{c,S}(\sigma). \tag{16}$$

Later, Danzer (1992) extended this distribution for inhomogeneous materials. Alternatively, Jayatilaka and Trustrum (1977) proposed a model based on flaw size distribution and material strength:

$$N(\sigma, V) = N\frac{c^{n-1}}{n!}\left(\frac{\pi\sigma^2}{K_{IC}^2}\right)^{n-1} \tag{17}$$

where N is the number of cracks, K_{IC} is the critical stress intensity factor of the material, and n and c are characteristic constants. The above mentioned models assume that there is no interaction between defects. However, Afferrante et al. (2006) demonstrate that the Weibull distribution of material strength applies in a general sense, even if there is interaction between the defects. They also note that the Weibull modulus does not necessary correspond to a material constant, and that it may be influenced by the interaction among

cracks, or the interaction of cracks and the stress field. Thus, in the examples we investigate in Sect. 5, we will use the Weibull distribution (12) and will vary the Weibull modulus to illustrate its influence on the global fracture behavior. Although it is recognized that a spatial correlation may exist in the strength of a material, no presumption of such a correlation is made in the examples presented in Sect. 5.

4 Unstructured geometry by means of nodal perturbation

The most popular technique for discretizing a volume into tetrahedral elements may be the Delaunay triangulation (Lo 1991; Delaunay 1934; Cavendish et al. 1985; Schroeder and Shephard 1988). Delaunay triangulation is the technique of choice for most automatic mesh generators (Schröberl 1997; Geuzaine and Remacle 2009). However, automatic mesh generators often conduct additional post-processing of the mesh; to remove elements with degenerate edges and sliver elements. In some cases this additional post-processing leads these (initially random) meshes to contain an underlying structure. To remove this structure, we propose using the technique of nodal perturbation (NP).

To implement the NP algorithm, we apply the following steps. First, all the nodes in the mesh are traversed and restrictions are placed on boundary nodes. Corner nodes are fixed, edge nodes are restricted to the original line of the edge and face nodes are restricted to the boundary face. At each node, the minimum distance between the node and the opposite faces of the adjacent tetrahedrons is computed. The node is then perturbed in a random direction; where the magnitude of the perturbation corresponds to the computed distance multiplied by a constant perturbation factor, NP ≤ 1. After perturbing the nodes, a Laplacian smoothing technique is used to improve the mesh quality (Field 1988; Paulino et al. 2010). In this step, each element in the mesh is visited and the quality of the element is assessed. The element quality is quantified by Lo's parameter (Lo 1991), γ:

$$\gamma = \frac{72\sqrt{3}\, V_{tetrahedron}}{\left(\sum \text{square of edges}\right)^{3/2}} \tag{18}$$

where $V_{tetrahedron}$ is the volume of the tetrahedron. Equivalently:

$$\gamma(A,B,C,D) = \frac{12\sqrt{3}\,(AB\times AC)\cdot AD}{\left(\|AB\|^2+\|BC\|^2+\|CA\|^2+\|AD\|^2+\|CD\|^2+\|BD\|^2\right)^{3/2}}. \tag{19}$$

where A, B, C, and D correspond to the nodal positions of the tetrahedron, and $\times$ and $\cdot$ correspond to the cross and dot products, respectively. The higher the Lo's parameter, the higher the quality of the element. For example, equilateral tetrahedra have a Lo's parameter of 1.0. If an element fails to meet a minimum specified Lo's parameter, the position of each node in the element is displaced by the average of the distance vectors to the neighboring nodes on the edges incident to the node (Paulino et al. 2010). This procedure is iterated until all elements in the mesh meet the minimum quality requirements.

Here, we conduct a series of geometric studies on a mesh before and after NP. The studies are conducted on a cubic domain randomly discretized with 47,924 tetrahedral elements, as illustrated in Fig. 4. An illustration of the effect of NP on a typical Delaunay mesh is shown in Fig. 4b–d. The NP factors used in this study range from 0.1 to 0.6 in increments of 0.1. Three unique meshes are generated for each random NP factor, and the results of the studies are averaged. To quantify the effect of NP, we track three metrics: element quality (Lo's parameter), minimum interior angle and maximum interior angle.

The desired average mesh quality parameter is selected as 0.7; which is generally acceptable for finite element simulations (Paulino et al. 2010). The minimum Lo's parameter for an unperturbed mesh is 0.434, and decreases with increasing NP factor. A histogram of the mesh quality for increasing NP factors is illustrated in Fig. 5. As the NP factor increases, the range of Lo's parameters broadens and skews to lower values. Regardless of the NP factor, the maximum Lo's parameter is approximately 1.0.

To gain additional insight into the influence of NP on the mesh, we investigate the minimum and maximum interior angles in the elements. The interior angles can give insight into the initial distortion of the elements. For example, the commercial software Abaqus qualifies elements with interior angles less than 10° or greater than 160° as distorted (ABAQUS 2011). A histogram of the minimum interior angle is presented in Fig. 6a, while one for the maximum interior angle is presented in Fig. 6b. For the unperturbed case, the smallest minimum interior angle is approximately

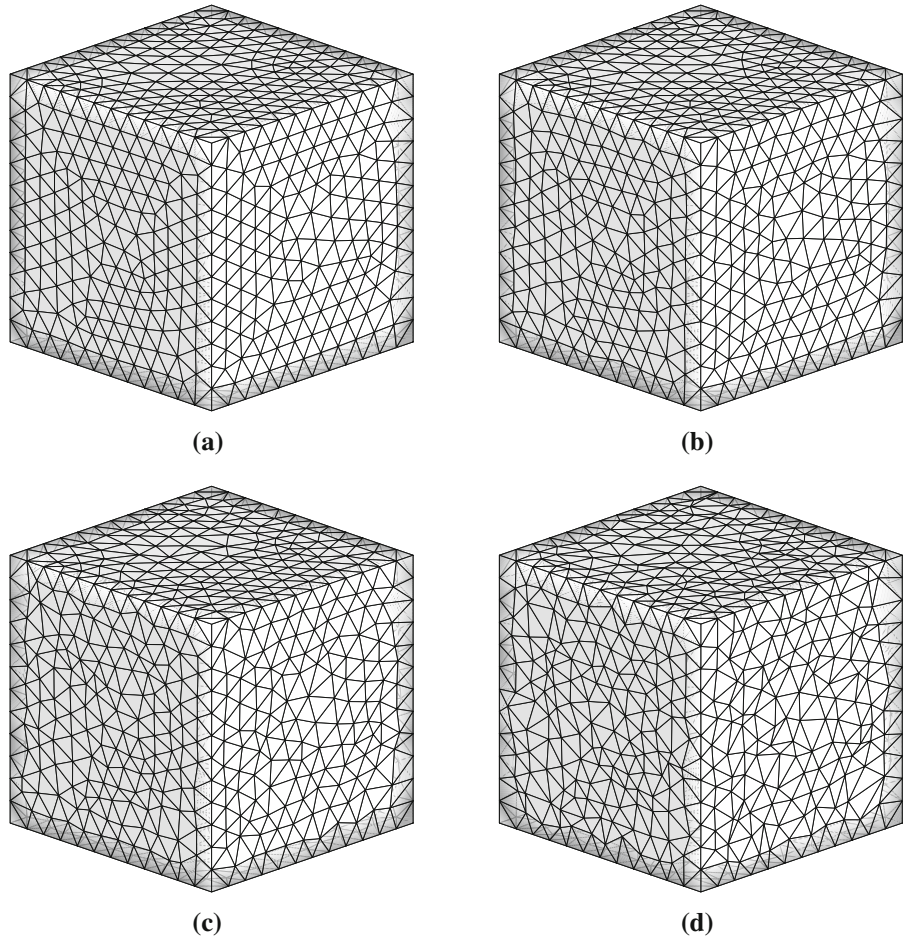

Fig. 4 Influence of nodal perturbation on meshes generated using a Delaunay triangulation (Schröberl 1997). **a** Unperturbed, **b** nodal perturbation factor of 0.2, **c** nodal perturbation factor of 0.4, and **d** nodal perturbation factor of 0.6

25.3°, and decreases with increasing NP factor. Similarly, the largest maximum interior angle for the unperturbed case is approximately 120.7° and increases with increasing NP factor. These results are in line with expectations, as perturbing the nodes distorts the elements and the higher the perturbation factor the higher the level of distortion.

A summary of the results of the geometric study is presented in Table 1. Based on the results of the study, the NP factor of 0.4 is determined to be the maximum factor which still maintains a high quality mesh and conforms to the recommended interior angles (ABAQUS 2011). Thus, this is the NP factor we use in the remainder of the paper.

The above-mentioned geometric studies discuss the influence of the nodal perturbation factor on the quality of the mesh, but some comments can be made on the influence of the nodal perturbation factor on the stable time step. When conducting a dynamic fracture simulation, the time step is controlled by the Courant-Friedrichs-Lewy (CFL) stability condition (Bathe 1996):

$$\Delta t \leq \frac{l_e}{C_d} \tag{20}$$

where l_e is the shortest distance between any two nodes in the mesh, and C_d is the dilatational wave speed of the material. Typically, the time step is recommended to be further reduced to 10% of that required by the CFL condition, when conducting a dynamic fracture simulation (Zhang 2003). The nodal perturbation technique does increase the coefficient of variation for element facets and thus increases the likelihood for a small, time-step-controlling facet to be introduced to the mesh. However, since the meshing algorithms considered here are random Delaunay triangulations, there is always a chance that there could be a small edge introduced, regardless of whether or not nodal perturbation is used. Thus,

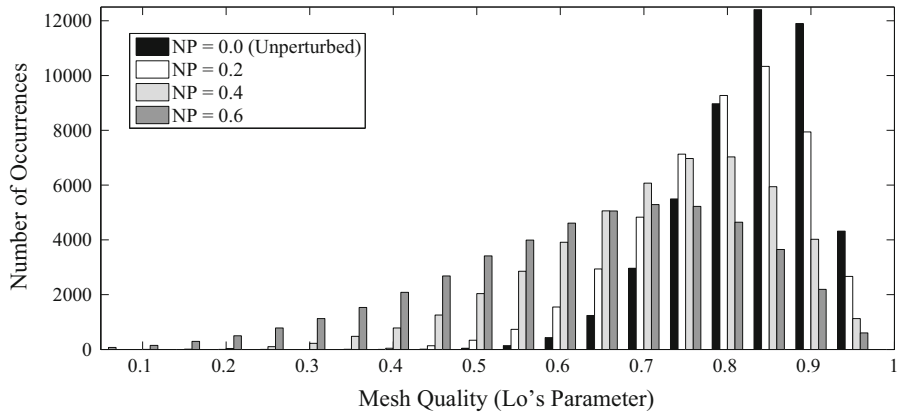

Fig. 5 Histograph of mesh quality for various nodal perturbation factors

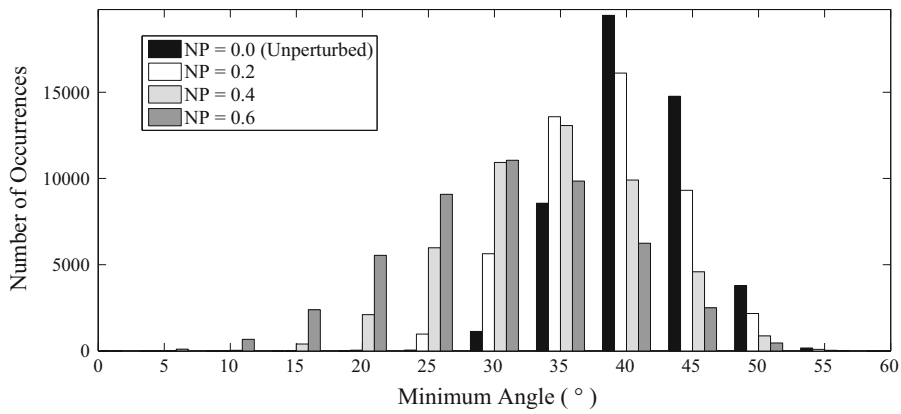

(a)

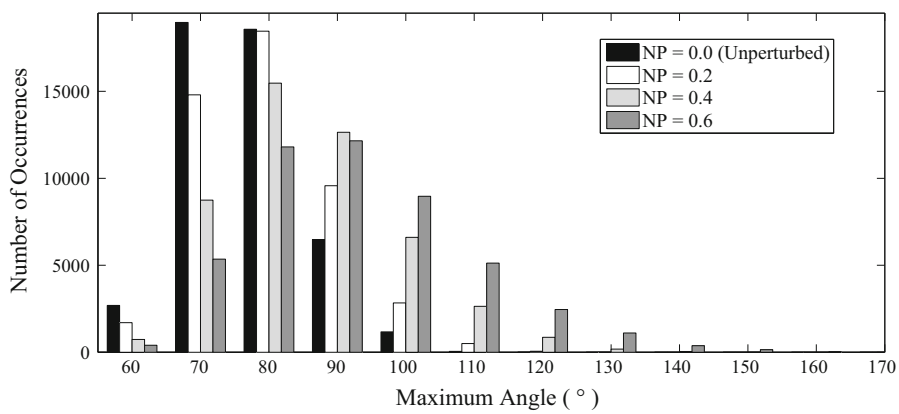

(b)

Fig. 6 Results of the study on the interior angles in the mesh: **a** histograph of minimum angles, and **b** histograph of maximum angles

the assessment of the time step must be conducted on a case-by-case basis. For the mesh investigated here, containing 47,924 linear tetrahedral elements, the smallest facet was calculated to be approximately twice as small when a nodal perturbation factor of 0.4 was used, compared to when no nodal perturbation was used.

5 Examples

In this section, three example problems are investigated. The first example considers the centrifugal loading of a spinning disk. The second example investigates the impulse loading of a hollow sphere, with a focus on the influence of surface features on the fragmentation

Table 1 Summary of the results for the mesh quality study

	Lo's parameter (γ)			Minimum angle (°)			Maximum angle (°)		
NP factor	Min	Mean	Max	Min	Mean	Max	Min	Mean	Max
0.0	0.434	0.858	0.999	25.3	43.7	58.1	61.5	81.8	120.7
0.1	0.419	0.848	0.998	24.3	43.0	58.4	61.9	82.6	123.1
0.2	0.292	0.820	0.998	19.9	41.1	58.1	62.0	84.8	132.5
0.3	0.225	0.782	0.997	15.2	38.8	57.9	62.5	87.8	142.0
0.4	0.132	0.738	0.996	11.5	36.5	57.3	62.5	90.9	152.4
0.5	0.064	0.695	0.996	7.2	34.4	57.6	63.3	94.2	162.7
0.6	0.027	0.656	0.998	3.7	32.6	58.0	61.6	97.1	171.0

The quantities for each metric are averaged over three random instances

behavior of the sphere. The third example considers the fragmentation of a kidney stone under direct impact. Since kidney stones often display a radial gradation of material properties, we consider both homogeneous and functionally graded materials. Unless noted otherwise, we consider a fragment to be a mass of bulk elements (and cohesive elements which have not fully separated) completely surrounded by boundary facets and/or fully separated cohesive elements. A pseudo code of the procedure we use to determine the fragments is provided in Appendix A. For each example, a mesh refinement study was conducted such that the number of fragments whose volume exceeded 1% of the volume of the model converged, for the case of a homogeneous material. For a more rigorous and in-depth discussion on the challenges and issues related to the mesh convergence of models for fragmentation simulation, the interested reader is referred to Bishop and Strack (2011) and Bishop et al. (2016). Comparisons to experiments are made where possible. In all of the examples, we consider the influence of a randomly assigned cohesive strength on the fragmentation behavior. The Weibull function (12) is selected to describe the distribution of cohesive strength, with the volume parameter assumed to be equal to 1.0 (Danzer 1992). The impact of the volume parameter on fracture patterns has been discussed elsewhere by Brannon et al. (2007).

5.1 Centrifugal loading of a spinning disk

This example considers the fragmentation of a spinning disk; which is motivated by the use of structural ceramics in the high stress environment of a spinning turbine. We consider two different geometries for the disk, as illustrated in Fig. 7. The two disks, from this point forward, will be referred to as the small disk and the large disk, respectively. Each disk is ceramic, constituted of silicon nitride (Si_3N_4); the elastic modulus of which is 300 GPa, the Poisson's ratio is 0.3, and the density is 3250 kg/m^3. The mode I fracture energy (ϕ_n) and shape parameter (α) are set as 180 N/m and 2, respectively. The minimum cohesive strength, σ_{min}, is set as 425 MPa. Two Weibull moduli, $m = 2, 5$ and two scale parameters $\lambda = 40$ MPa, 80 MPa are considered. The mode II fracture properties are assumed to be the same as the mode I fracture properties. The mean, median and variance of the cohesive strength for each case is listed in Table 2.

Experimentally, the small disk specimen was investigated by Swank and Williams (1981); however, to the best of the author's knowledge, there have been no numerical investigations using this geometry and loading condition. To simulate this problem, we use a randomly generated mesh containing 124,882 linear tetrahedral elements (30,421 nodes), and a NP factor of 0.4. The spinning of the disk is represented as a centrifugal force (applied as a body force), with an angular velocity of $4\pi \times 10^3$ rad/s. The angular velocity is ramped up linearly over 100 μs and held constant thereafter. For each Weibull modulus (m) and scale parameter (λ) we run three simulations (a total of 12 simulations). For this example, we illustrate each of the results in Fig. 8. Each result displays the final fragmented shape of the specimen.

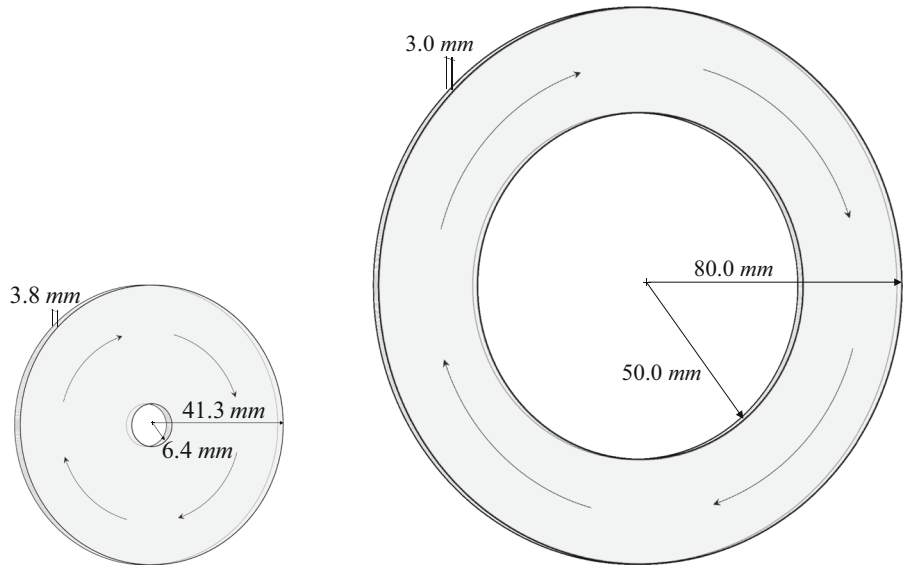

Fig. 7 Geometries investigated in the spinning disk example: **a** small disk, and **b** large disk

Table 2 Summary of the cohesive strengths used in the analysis of the spinning disks

Scale parameter (λ) (MPa)	Weibull modulus (m)	Mean strength (MPa)	Median strength (MPa)	Variance (MPa)
40	2	460.5	458.3	343.4
40	5	461.7	462.2	70.8
80	2	495.9	491.6	1373.5
80	5	498.5	499.3	283.1

Based on the results, it is clear that the random distribution of material properties, and the random perturbation of nodes, produces a random result in each simulation. However, qualitatively there are many similarities among the fracture patterns. For the most part, the small disk specimen fractures into approximately four large fragments and 1–3 medium fragments. The large fragments are defined as the bulk of material between two cracks which span the entire thickness of the disk. A medium fragment is defined as the bulk of material that results after the branch of a through-thickness crack reaches the outer boundary of the specimen. For example, the result illustrated in Fig. 8f displays four large fragments and two medium fragments. In addition to the qualitative fracture patterns, we also calculate the crack speed through the specimen. The crack speed is determined by simply documenting the time it takes for a crack to propagate through the entire width of the disk. A summary of the results is presented in Table 3.

The crack velocity varies between 2769 and 3181 m/s, depending on the distribution of material strength. For the wider distribution of strength, $m = 5$, the crack velocity is higher than that observed for a more homogeneous, or narrow, distribution of strength, $m = 2$. The Rayleigh wave speed, C_R, for Si_3N_4 is 5600 m/s, thus the computed values fall in the range of $0.49C_R$ to $0.57C_R$; which is consistent with the experimentally expected crack velocity.

The large disk specimen was investigated experimentally by Hashimoto et al. (1996). Numerically, this problem has been simulated by Zhou and Molinari (2004). They simulate fracture using a linear cohesive traction-separation relation, and also consider the influence of material heterogeneity. Their investigation determined that the greater the heterogeneity in the material (i.e. the wider the range of cohesive strength), the fewer fragments produced. In addition, they compute an average crack velocity of 5500 m/s, or 98%

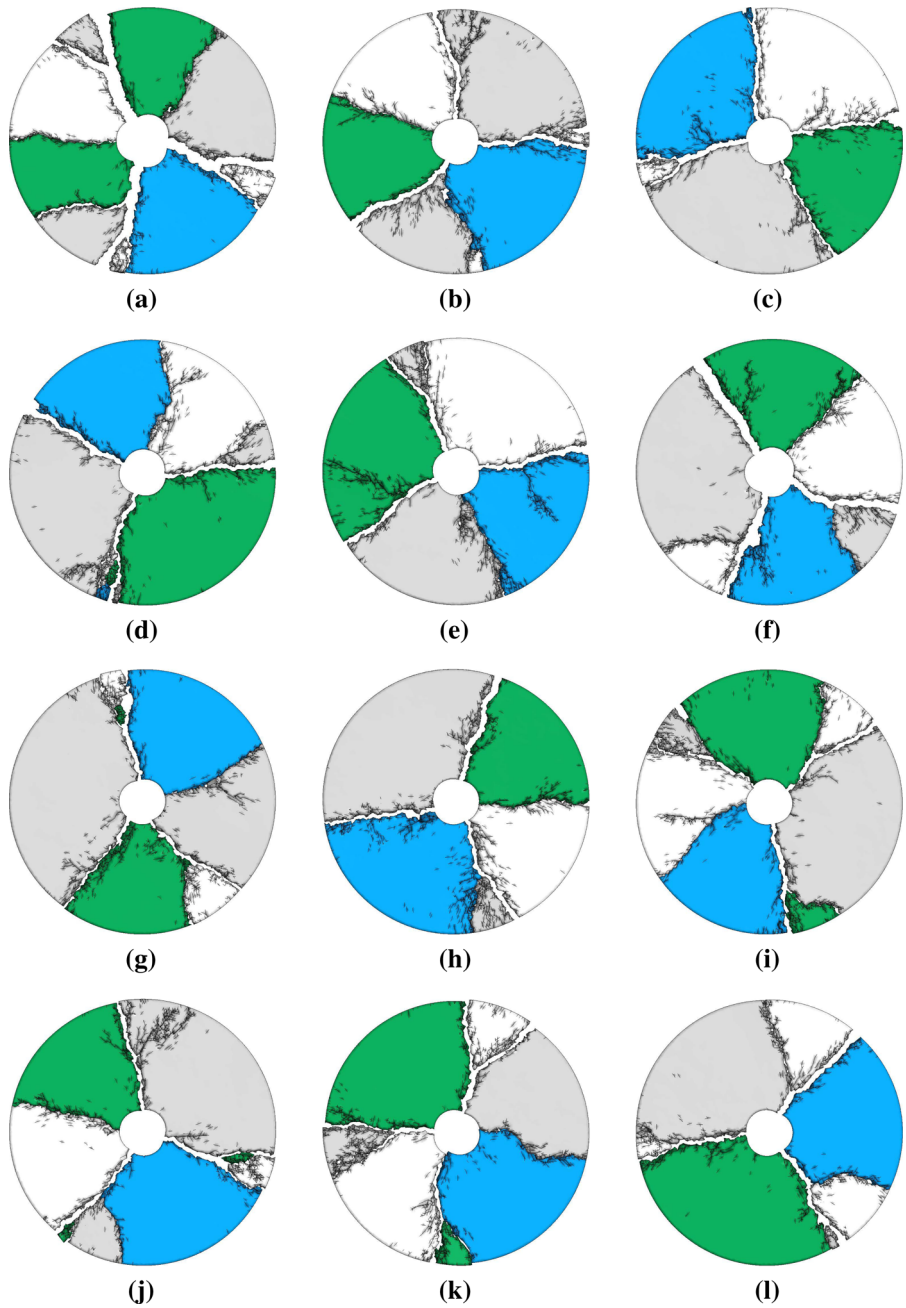

Fig. 8 Results for the small disk geometry with Weibull parameters: **a-c** $\lambda = 40$ MPa, and m = 2; **d-f** $\lambda = 40$ MPa, and m = 5; **g-i** $\lambda = 80$ MPa, and m = 2; and **j-l** $\lambda = 80$ MPa, and m = 5. All the results are illustrated in their final fragmented form, which occurred in the range of 118–127 μs. For visual clarity, the small fragments (those comprised of fewer than 10 bulk elements) have been removed from the displayed results

of the Rayleigh wave speed; a result which they note is inconsistent with experiments (Zhou and Molinari 2004).

To simulate this problem, we use a model containing 140, 339 elements (40,768 nodes). Similarly to the small disk, we represent the spinning of the large disk as a centrifugal force, with an angular velocity of $2.8\pi \times 10^3$ rad/sec. The angular velocity is ramped up linearly over 100 μs and held constant thereafter. For each Weibull modulus (m) and scale parameter (λ) we run three simulations (a total of 12 simulations). For this example, we only illustrate a typical result for each combination of Weibull modulus and scale parameter in Fig. 9. Each result displays the final fragmented shape of the specimen. The resulting number of large and medium fragments is summarized in

Table 3 Summary of the small disk results

Scale parameter (λ) (MPa)	Weibull modulus (m)	Large fragments	Medium fragments	Crack velocity (m/s)
40	2	4.33	2.67	2888
40	5	4.00	2.67	3181
80	2	4.00	2.33	2769
80	5	3.67	3.33	3179

Each result is the average of three simulations
A large fragment is defined as the bulk of material between two cracks which span the entire thickness of the cylinder. A medium fragment is defined as the bulk of material that results after the branch of a through-thickness crack reaches the outer boundary of the specimen

Table 4. For the smaller scale parameter, $\lambda = 40$ MPa, a greater number of large and medium fragments is produced than in the case with a larger scale parameter, $\lambda = 80$ MPa. Overall, the fracture patterns correspond well to those observed experimentally (see Fig. 4 in Hashimoto et al. 1996), and the distribution of fragments corresponds well to those in alternate numerical investigations (Zhou and Molinari 2004).

The velocity of the through-thickness cracks is also tracked, and the results are included in Table 4. The crack velocity varies between 3165 and 3390 m/s, depending on the distribution of material strength. Similar to the small disk geometry, for a wider distribution of strength, $m = 5$, the crack velocity is higher than that observed for a more homogeneous distribution of strength, $m = 2$. For comparison, the computed values fall in the range of $0.56C_R$ to $0.61C_R$.

5.2 Impulse Loading of a Hollow Sphere

This example investigates the fragmentation of a hollow sphere loaded with a radial impulse. We consider both a smooth sphere (Fig. 10) and a sphere containing surface features (Fig. 11). Numerically, the smooth sphere geometry was investigated by Levy (2010) and Vocialta et al. (2016). Levy investigated the effect of the thickness of the sphere on the shape and distribution of fragments while Vocialta et al. extended Levy's work for parallel implementation. In this study, we set the inner radius of the sphere to be 9.25 mm, and the outer radius to be 10 mm, as illustrated in Fig. 10a. The geometry is discretized with approximately 100,000 linear tetrahedral elements (approximately 25,000 nodes), as illustrated in Fig. 10b. The sphere is constituted of aluminum oxide (Al_2O_3); the elastic modulus of which is 370 GPa, the Poisson's ratio is 0.22, and the density is 3900 kg/m^3. The mode I fracture energy and shape parameter are set as 50 N/m and 2, respectively. The minimum cohesive strength, σ_{min}, is set as 264 MPa. Two Weibull moduli, $m = 2, 5$, and two scale parameters $\lambda = 50$ MPa, 100 MPa are considered. The mean, median and variance of the cohesive strength for each case is listed in Table 5.

The sphere is loaded with a radial impulse. Since we assume the sphere to be centered on the origin, the initial nodal velocities are prescribed as:

$$v_x(x, y, z) = \dot{\varepsilon}x, \quad v_y(x, y, z) = \dot{\varepsilon}y, \quad \text{and} \quad v_z(x, y, z) = \dot{\varepsilon}z, \tag{21}$$

where x, y, and z, are the nodal coordinates, and $\dot{\varepsilon}$ is the applied rate of strain. In this study we will consider two different strain rates, $\dot{\varepsilon} = 2500\,\text{s}^{-1}$ and $\dot{\varepsilon} = 5000\,\text{s}^{-1}$. Once again, for each geometry, loading rate, Weibull modulus and scale parameter, we run three simulations (a total of 72 simulations). For visual clarity, the fragments will be individually colored in each of the results we illustrate.

For a strain rate of $\dot{\varepsilon} = 2500\,\text{s}^{-1}$, we illustrate some typical results in Fig. 12 for a Weibull modulus of $m = 2$ and scale parameter $\lambda = 50$ MPa. As shown in Fig. 12a, the smooth sphere fragments into large pieces with no discernible pattern. Alternatively, each case with surface features displays a distinct pattern by which it fragments. For the case with surface dimples, fracture was observed to initiate at the centroid of the dimples and to radiate outwards, as illustrated in Fig. 13. This is not surprising,

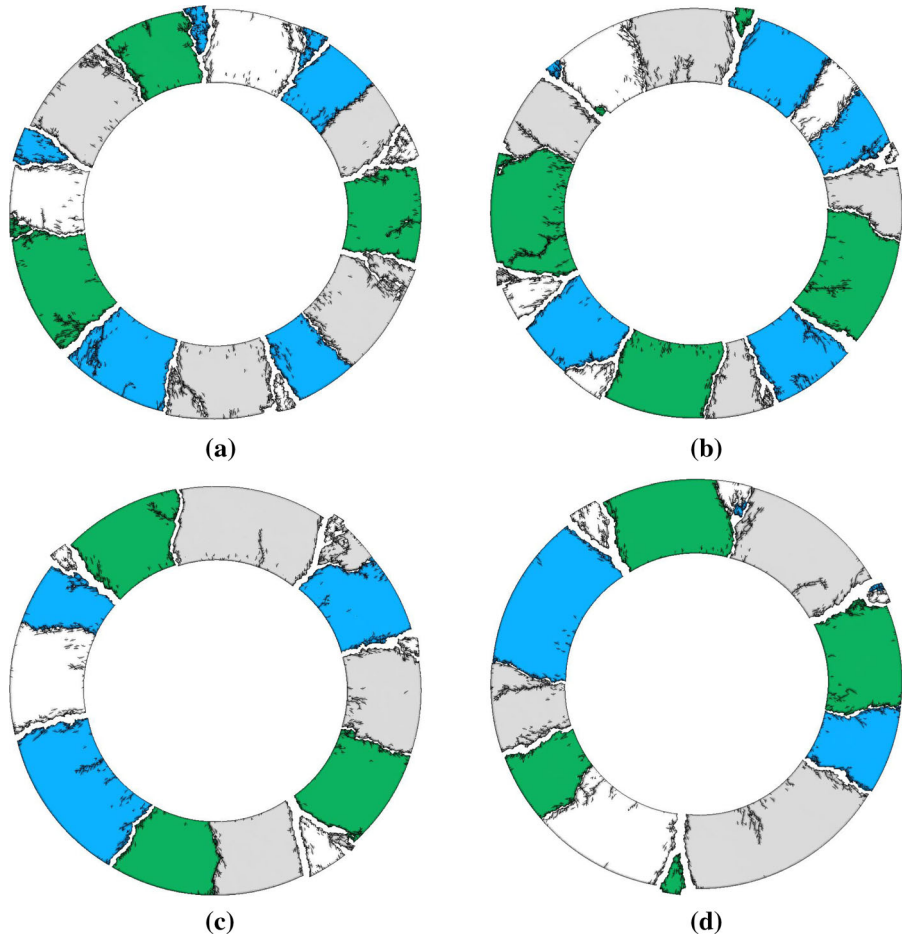

Fig. 9 Typical results for the large disk geometry with Weibull parameters: **a** $\lambda = 40$ MPa, and $m = 2$; **b** $\lambda = 40$ MPa, and $m = 5$; **c** $\lambda = 80$ MPa, and $m = 2$; and **d** $\lambda = 80$ MPa, and $m = 5$. All the results are illustrated in their final fragmented form, which occurred at approximately 87 μs. For visual clarity, the small fragments (those comprised of fewer than 10 bulk elements) have been removed from the displayed results

Table 4 Summary of the large disk results

Scale parameter (λ) (MPa)	Weibull modulus (m)	Large fragments	Medium fragments	Crack velocity (m/s)
40	2	12.33	6.67	3165
40	5	13.67	7.00	3390
80	2	11.33	4.33	3203
80	5	10.67	5.67	3346

Each result is the average of three simulations

A large fragment is defined as the bulk of material between two cracks which span the entire thickness of the cylinder. A medium fragment is defined as the bulk of material that results after the branch of a through-thickness crack reaches the outer boundary of the specimen

as the geometry is thinnest at this location, causing stresses to concentrate here. Additionally, the placement of the dimples appears to control the geometry of the fragments. In Fig. 12b, one can see that the edges of the fragments align with neighboring dimples. When we consider the case with bumps (Fig. 12c) there is clear evidence that the edges of the fragments are deflected away from the bumps. Thus, the bumps remain intact during fragmentation. While we only display selected results here, this behavior was shown

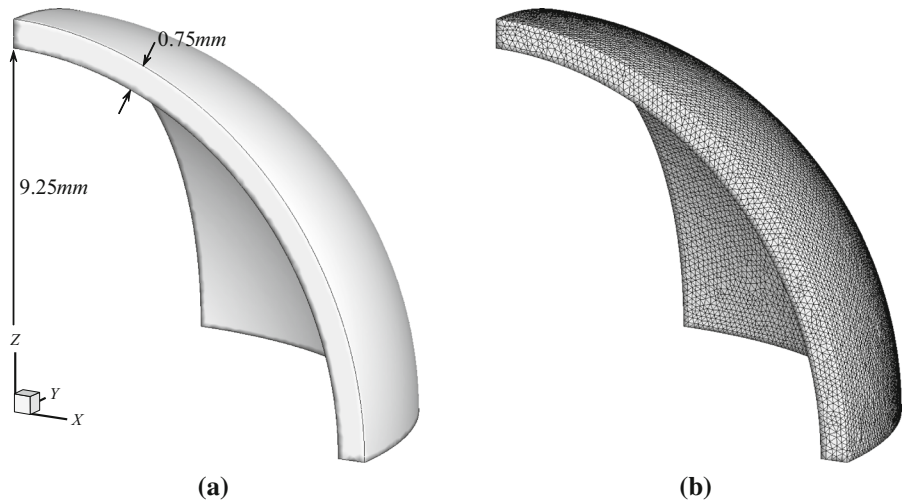

Fig. 10 Model of a smooth, hollow sphere; **a** geometry, and **b** mesh

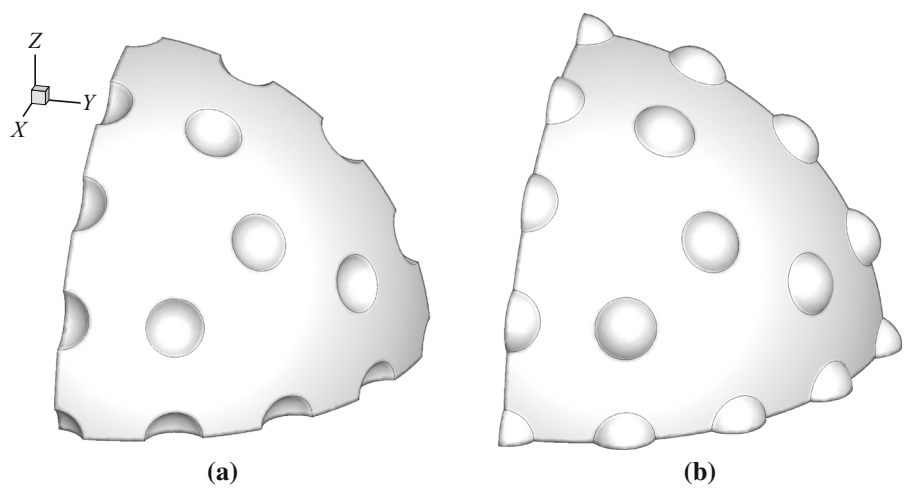

Fig. 11 Geometry of a hollow sphere with different surface features, **a** dimples, and **b** bumps. The dimples are generated by removing material that intersects with spheres of radius, $r = 1.1$ mm, placed at a radial distance of 10.5 mm from the origin. The bumps are generated through the union of the smooth sphere and spheres of radius, $r = 1.1$ mm, placed at a radial distance of 9.5 mm from the origin

Table 5 Summary of the cohesive strengths used in the analysis of the hollow sphere

Scale parameter (λ) (MPa)	Weibull modulus (m)	Mean strength (MPa)	Median strength (MPa)	Variance (MPa)
50	2	308.3	305.6	536.5
50	5	309.9	310.5	110.6
100	2	352.6	347.3	2146.0
100	5	355.8	356.9	442.3

across all the Weibull moduli and scale parameters we considered.

If we increase the applied strain to $\dot{\varepsilon} = 5000\,\mathrm{s}^{-1}$, fragmentation becomes more pervasive, as illustrated in Fig. 14. Similar to the previous case, the fragmentation of the smooth sphere does not display any discernible pattern. However, fracture continues to initiate at, and to radiate outwards from, the dimples; and each bump is wholly contained in a single fragment. Once again, this behavior was shown across all the Weibull moduli and scale parameters we considered.

To further examine the fragmentation behavior, we plot the evolution of fragmentation through time in Fig. 15. Results are shown for a variation in scale

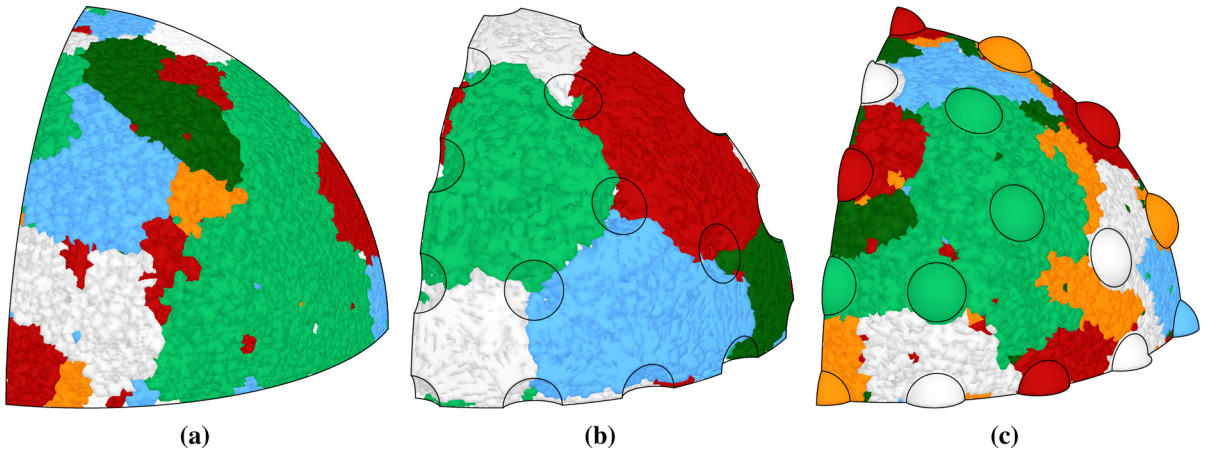

Fig. 12 Final fragmented geometries, after impacted with an impulse load at a rate of $\dot{\varepsilon} = 2500\,\mathrm{s}^{-1}$, for: **a** a smooth sphere, **b** a sphere with dimples, and **c** a sphere with bumps. The results show typical fracture patterns, but are for the case with $\lambda = 50$ MPa and $m = 2$. The fragments are colored for visual clarity, and the small fragments (those comprised of fewer than 10 bulk elements) have been removed from the displayed results

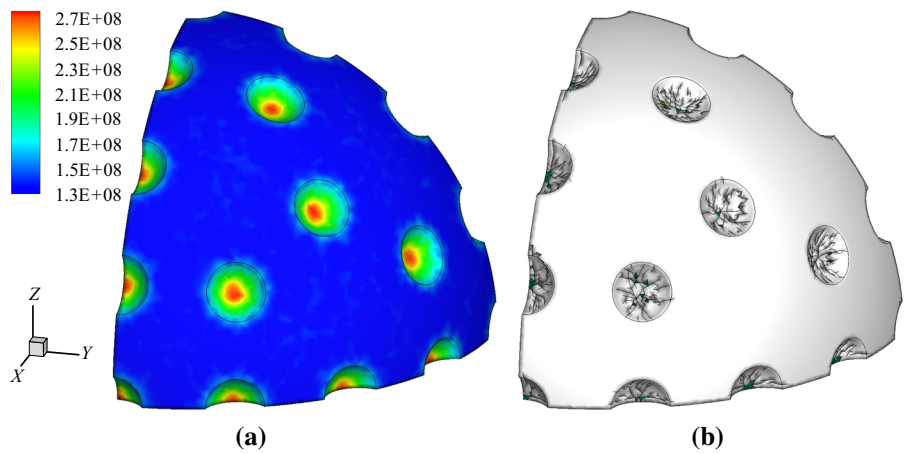

Fig. 13 Initial stages of fracture in a sphere with dimples. **a** Contour of principal stress, illustrating the concentration of stress at the centroids of the dimples, immediately prior to fracture; and **b** fracture initiating at the dimples

parameter, λ, with a constant Weibull modulus of $m = 2$. In each scenario, fragmentation initiates quickly (after approximately 0.5 to 2 μs), and takes approximately 20 μs to complete. In all the cases with a higher applied rate of strain, $\dot{\varepsilon} = 5000\,\mathrm{s}^{-1}$, the majority of the fragmentation occurs in the first 10 μs, and fragmentation evolves slower in cases with $\lambda = 100$ MPa than they do in cases with $\lambda = 50$ MPa. When we examine the cases with a lower rate of strain, $\dot{\varepsilon} = 2500\,\mathrm{s}^{-1}$, little difference is observed in the cases with $\lambda = 50$ MPa and $\lambda = 100$ MPa. However, for the case with dimples (Fig. 14b) fragmentation evolves at a faster rate than when we consider a smooth sphere, or a sphere with bumps. From this investigation, we see that the distribution of material parameters does have an impact on the manner in which fragmentation occurs; however, the fragmentation patterns are also significantly influenced by surface features. This investigation provides support to the idea of being able to control fragmentation behavior through simple design features.

An investigation of energy evolution is conducted for the case of the smooth sphere, as illustrated in Fig. 16. The energy is comprised of the strain (E_{int}), kinetic (E_{kin}) and fracture (E_{fra}) energies. The impulse load on the structure results in a large initial kinetic energy, which is converted into strain energy in the system. The fracture energy remains equal to zero up until the point of crack initiation, and monotoni-

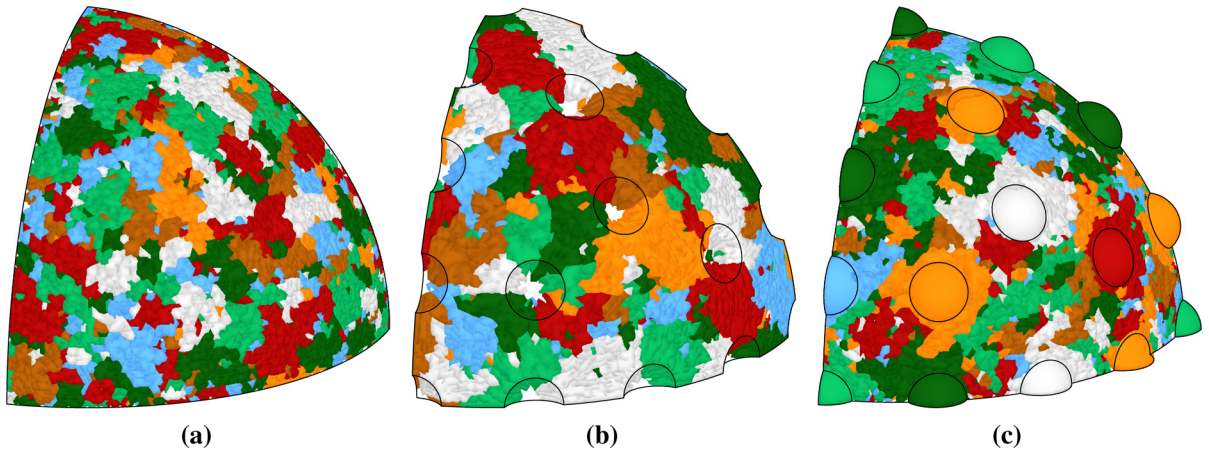

Fig. 14 Final fragmented geometries, after impacted with an impulse load at a rate of $\dot{\varepsilon} = 5000\ \mathrm{s}^{-1}$, for: **a** a smooth sphere, **b** a sphere with dimples, and **c** a sphere with bumps. The results show typical fracture patterns, but are for the case with $\lambda = 50$ MPa and $m = 2$. The fragments are colored for visual clarity, and the small fragments (those comprised of fewer than 10 bulk elements) have been removed from the displayed results

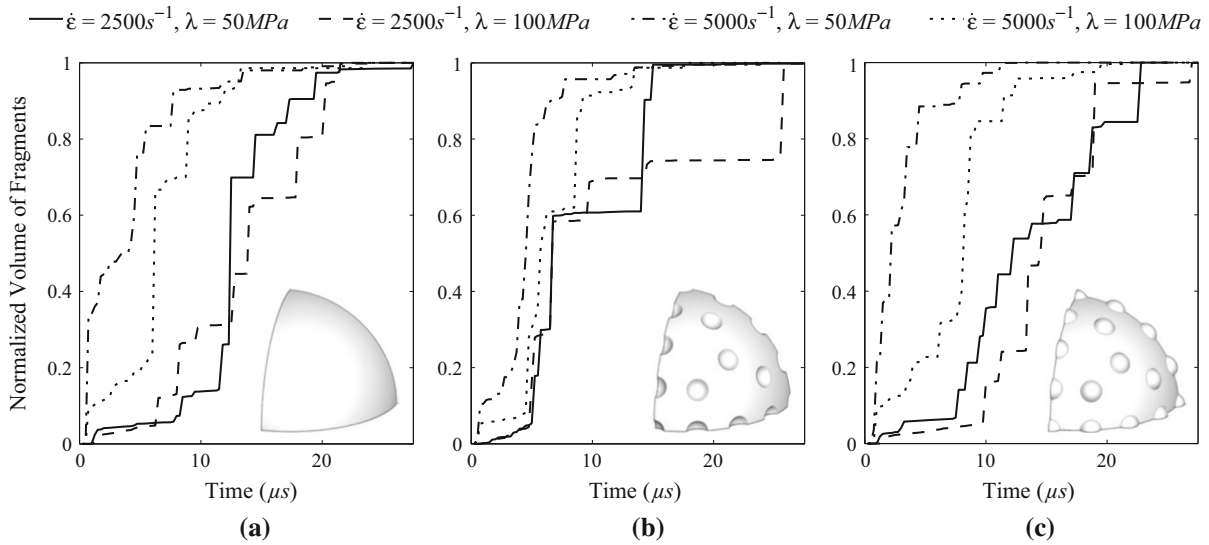

Fig. 15 Evolution of fragmentation for: **a** a smooth sphere, **b** a sphere with dimples, and **c** a sphere with bumps. The results shown consider a Weibull modulus of $m = 2$

cally increases over time. The summation of energy in the system remains constant over time, indicating a conservation of energy. For a higher rate of strain, the initial kinetic energy in the system is larger, as illustrated in Fig. 16b. This higher rate of strain also leads to an earlier onset of fracture, however, the relative magnitudes of potential and fracture energy in each system remains unchanged.

While not pursued here, this example motivates a deeper investigation into the effects of surface features on fragmentation patterns and distributions. The fragmentation patterns illustrated here indicate a strong dependence on the kind of surface feature, but it is also likely that the fragmentation patterns would be a function of the spacing and sizing of each surface feature. Statistically quantifying such a functional dependence

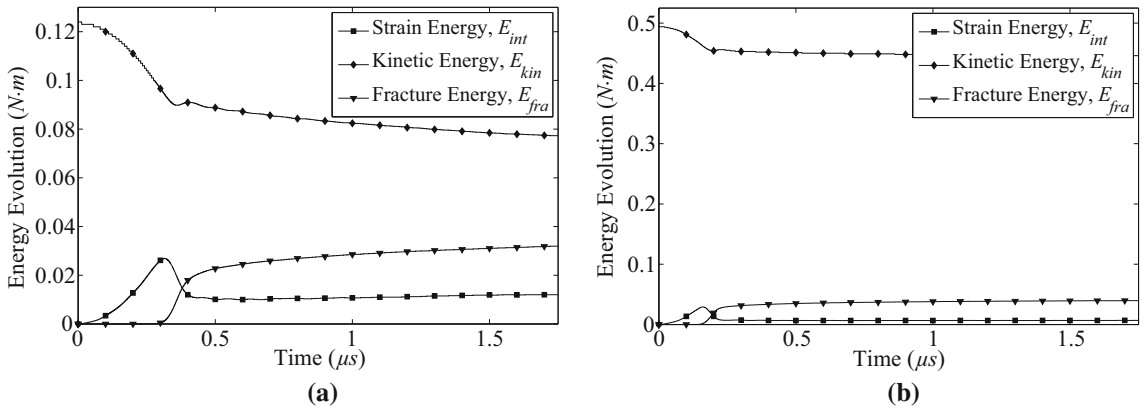

Fig. 16 Evolution of energy for a hollow sphere under an impulse load with an applied rate of strain of: **a** 2500 s^{-1}, and **b** 5000 s^{-1}

of the distribution of fragments on surface features may be pursued as a future work.

5.3 Direct impact of a kidney stone

This example considers the direct impact of a kidney stone through the use of a Lithoclast. The Lithoclast is a surgical tool which propels a metallic probe against the stone. The kinetic energy of the probe is dissipated throughout the stone, forming cracks and fragments, allowing for easier removal or passage. The structure of the kidney stone has long been known to be nonhomogeneous (Zhong et al. 1992, 1993; Pittomvils et al. 1994), however, most attempts at simulating such problems have assumed continuous material properties (Mota et al. 2006; Caballero and Molinari 2010, 2011). Mota et al. (2006) studied the fragmentation of manufactured, cylindrical kidney stones made from gypsum. They load the stone using the technique of Lithotripsy, wherein a pulse of pressure is applied to the exterior of the stone. They also conducted experiments and displayed the cohesive element method's ability to capture fragmentation patterns which agreed with those observed experimentally. Caballero and Molinari (2010) and Caballero and Molinari (2011) simulate the direct impact of the kidney stone through the Lithoclast, but only considered the simplified case of a homogeneous stone structure. In this example, we investigate the influence of a radially heterogeneous microstructure within the stone, and include the influence of randomly distributed material strength.

The model we use to simulate this problem has a radius of 10mm and contains, contains 51,746 elements (10,424 nodes), as illustrated in Fig. 17. The elements at the site of impact have a maximum element size of 0.1 mm, and those in the bulk of the stone have a maximum size of 0.65 mm. In this investigation we will consider the three distinct sets of material properties listed in Table 6. We will first investigate the fragmentation behavior for a homogeneous stone; then consider the behavior when the core of the stone is comprised of a different material than the outer layer of the stone. The numerical framework described in Sect. 2 applies to both homogeneous and functionally graded materials. To numerically capture the linear gradation of the material between distinct zones, we use graded finite elements; which incorporate the material gradation at the size-scale of the element. There have been multiple methods designed to allow for graded material properties at the element scale (Santare and Lambros 2000; Kim and Paulino 2002), however, in this work, we use the generalized isoparametric method proposed by Kim and Paulino (2002). In the generalized isoparametric method the element shape functions are used to interpolate the material parameters from the Gauss points to the nodes. Between distinct zones we grade all bulk and cohesive material parameters, as well, we continue to assume a random distribution of cohesive strength.

The impact of the probe is described by displacing the nodes in the impact site by a prescribed velocity. The velocity of the probe is not known precisely, but we assume that it decreases monotonically. Caballero and Molinari (2010) and Caballero and Molinari (2011) suggest that the impact velocity follows the relation:

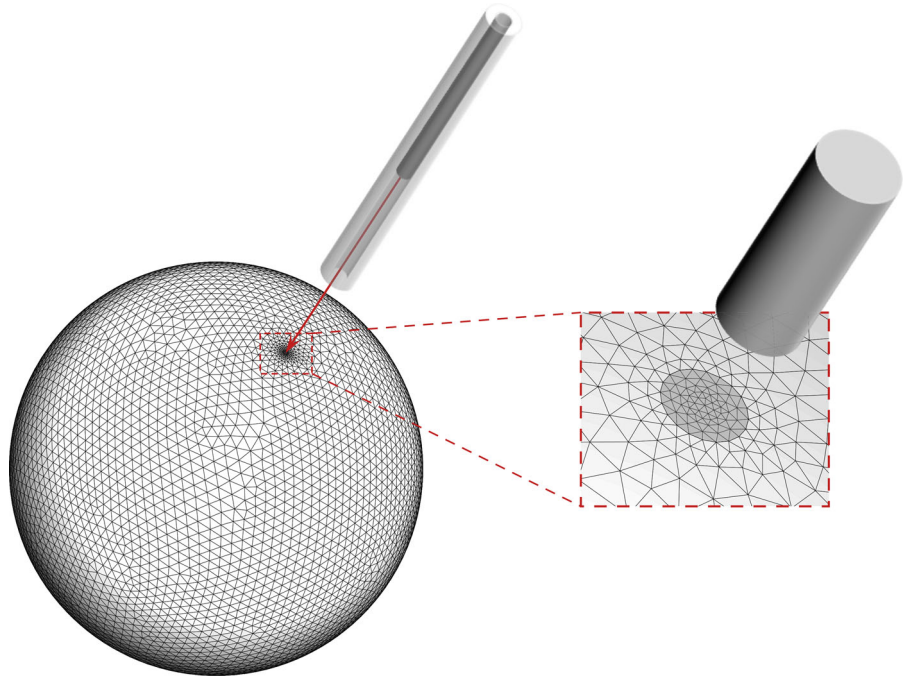

Fig. 17 Geometry and mesh of the kidney stone model

Table 6 Summary of material properties in common kidney stones

Stone composition (%)	ϕ (N/m)	σ (MPa)	ρ (kg/m^3)	E (MPa)
COM	0.735	1.500	2038	25.162
CA	0.382	0.500	1732	8.504
CA(50)/COM(50)	0.553	1.000	1885	16.833

COM calcium oxalate monohydrate; *CA* carbonate apatite (Zhong et al. 1993)

$$\dot{u}^C(t) = \dot{u}_0^C \left[1 - \frac{e^{-\eta \frac{t}{t_{max}}}}{1 + \left(e^{-\eta} - 1\right) \frac{t}{t_{max}}} \right], \tag{22}$$

where $\eta \in (-\infty, +\infty)$, $\dot{u}_0^C$ is the initial velocity of the probe, and t_{max} is the total time of contact. The total time of contact is determined through the following relation:

$$t_{max} = \frac{u_{t=t_{max}}}{\dot{u}_0^C} \frac{\left(e^{-\eta} - 1\right)^2}{1 - e^{-\eta}(1 + \alpha)}, \tag{23}$$

where $u_{t=t_{max}}$ is the maximum displacement achieved by the probe after impact. The velocity relation used in this investigation is illustrated in Fig. 18.

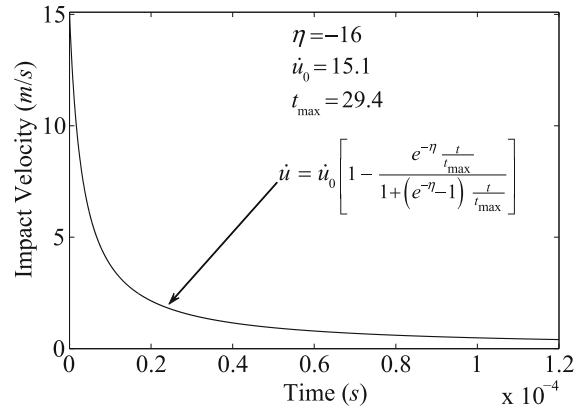

Fig. 18 Impact velocity of metal probe on kidney stone

First, we examine the fragmentation behavior of the homogeneous kidney stone. We consider all three materials listed in Table 6 and plot the evolution of fragmentation through time in Fig. 19. Results are shown for a variation in both scale parameter, λ, and Weibull

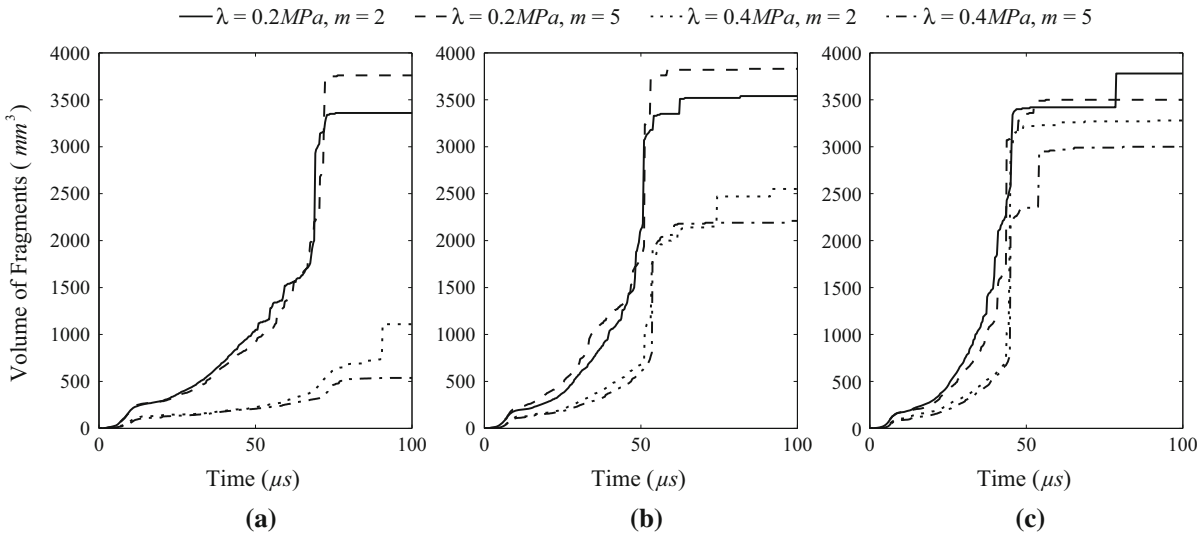

Fig. 19 Evolution of fragmentation for a homogeneous kidney stone constituted of: **a** CA, **b** CA(50)/COM(50), and **c** COM

modulus, m, for each material. In general, the fragmentation evolves slower for the most compliant material (CA), than it does for the least compliant material (COM). When considering the random distribution of material strength, the scale parameter is shown to have a much greater influence on the evolution of fragmentation that the Weibull modulus. For a smaller scale parameter, $\lambda = 0.2$ MPa, fragmentation occurs sooner and is more pervasive than in the case of a large scale parameter, $\lambda = 0.4$ MPa. Additionally, the final volume of fragments indicates that the stone does not fully fragment when the range of material strength increases. The results shown are for a single instance of the simulated results, however, each scenario was simulated three times, and the present results and conclusions are typical across each simulation.

When we assume that the stone contains a different constitutive make-up in the inner core than it does in the outer layer, the fragmentation behavior changes significantly. In this investigation, we consider scenarios with both a more compliant and less compliant material in the inner core. Based on experimental observations of the microstructure of kidney stones (Zhong et al. 1992, 1993; Pittomvils et al. 1994), the outer core was assumed to be 15% the thickness of the radius, and the zone transitioning between the inner core and outer layer was assumed to be 20% the thickness of the radius. Multiple values were investigated for the thickness of both the outer layer and zone of transition, but these values did not significantly influence the global response. Typical results are illustrated in Fig. 20. When we have a more compliant inner core, as in Fig. 20a, b, complete fragmentation evolves rapidly (in approximately 40–45 μs) regardless of the material in the core. Additionally, the distribution of material strength has a much smaller effect than in the homogeneous stones. Alternatively, when a less compliant material is present in the inner core, as in Fig. 20c, fragmentation is significantly restricted. The maximum volume of fragments produced was approximately 125 mm^3, significantly less than the volume of the stone (4189 mm^3). This small volume of fragments demonstrates the limited ability of the softer outer layer to transmit enough energy to the inner core, from the impacting probe, to cause fragmentation to occur. Similar behavior was observed across all scenarios we considered, including scenarios with different materials and thicker and thinner outer layers.

Similarly to the the previous example, we investigate the evolution of energy throughout the simulation. In this case, we examine the evolution of energy for two homogeneous materials, as illustrated in Fig. 21. In this example, the external energy from the impacting probe is converted into strain, kinetic and fracture energy. In the initial stages of impact, the external energy is pri-

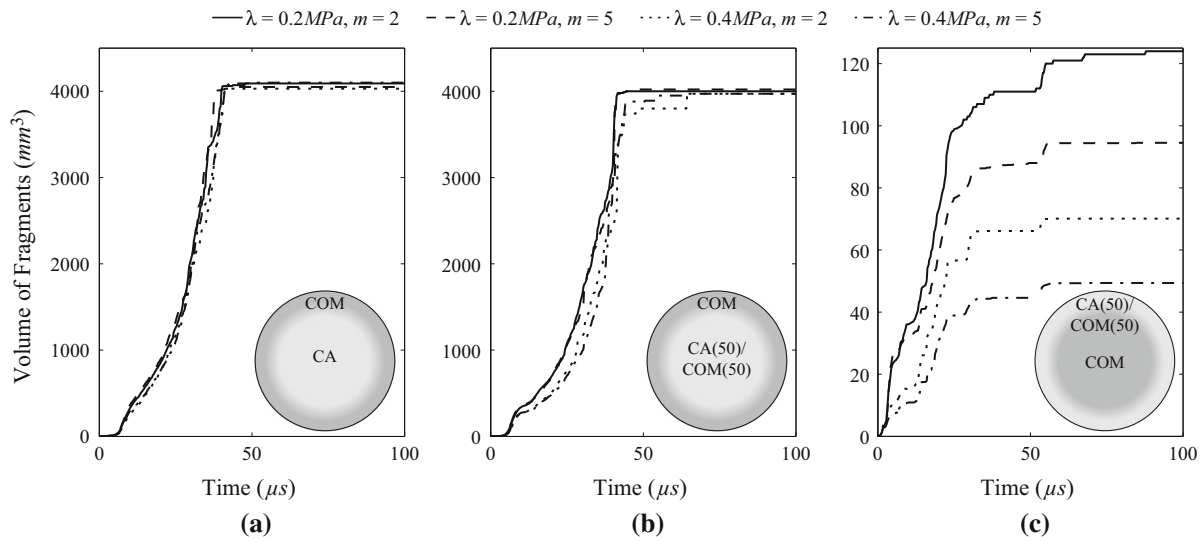

Fig. 20 Evolution of fragmentation for a graded kidney stone constituted of: **a** an inner core of CA, and an outer layer of COM; **b** an inner core of CA(50)/COM(50), and an outer layer of COM; and **c** an inner core of COM, and an outer layer of CA(50)/COM(50)

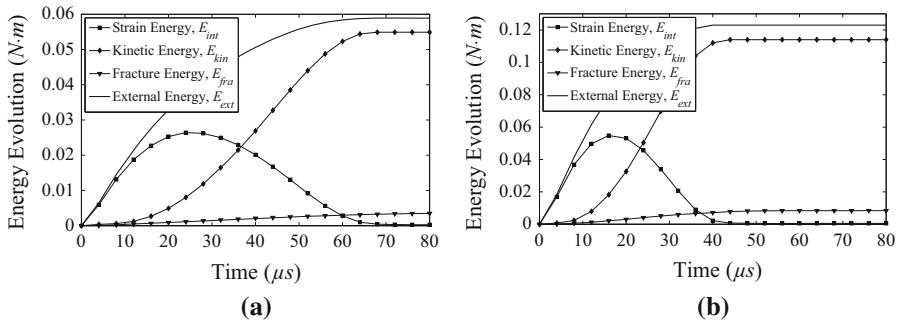

Fig. 21 Evolution of energy for a homogeneous kidney stone constituted of: **a** CA, and **b** COM

marily converted into strain energy. The strain energy increases rapidly, but decreases as the damaged region in the stone expands. As the stone begins to fracture, the kinetic energy and fracture energy increase. Over time, the problem reaches equilibrium, and the fracture of the stone stops. At equilibrium, the external energy is converted into kinetic and fracture energy, each of which remain constant with time.

6 Concluding remarks

The cohesive element method's ability to capture the full range of fracture behavior: from crack initiation, through crack propagation, branching and coalescence, all the way to complete fragmentation, has allowed us to study the pervasive fracture problems herein. In order to reduce mesh induced artifacts on fracture behavior, often caused by the use of smoothing operators in automatic mesh generators, we propose the nodal perturbation operator to introduce geometric randomness. We perform a geometric analysis on Lo's mesh quality parameter and minimum and maximum interior angles in the mesh before and after nodal perturbation. Through the investigation, we demonstrate that the use of a nodal perturbation factor around 0.4 is able to produce a highly randomized mesh while still maintaining high quality elements satisfying requirements on Lo's parameter and interior angles. Thus, this is the value of the nodal perturbation factor we recommend, and is the value used throughout the examples.

To further alleviate the influence of the mesh on the fracture patterns, we discuss the use of random heterogeneous constitutive relations. Random heterogeneous constitutive relations are motivated by the idea that no

material is truly homogeneous, but contains heterogeneities at the microscale. We provide a summary of many of the prominent methods, for representing these microscale heterogeneities, including the well-known Weibull distribution. We use these statistical means to distribute the strength of the material in the problems we investigate. To capture the failure response of the material, we implement the extrinsic PPR cohesive model, and adaptively insert cohesive elements in front of each crack tip to capture the nonlinear fracture behavior. This paper serves as an instance of the use of the extrinsic PPR model in three-dimensional fracture simulations.

Three numerical examples are presented, which are specifically selected to highlight many of the prominent features effecting the fragmentation of structures. The first example considers high-speed spinning of a ceramic disk. The combination of geometric and constitutive randomness results in random fracture behavior; which corresponds well to experimentally observed fragmentation patterns and crack speeds. The second example demonstrates the ability to use surface features on structures undergoing blast or impact loads to control fragmentation patterns. The third example demonstrates the significance of accounting for material gradation in the investigation of structures under direct impact. By using the case of a graded kidney stone, we demonstrate that the gradation of the material can significantly influence the fragmentation behavior, and in some cases can even inhibit fragmentation from occurring altogether.

Acknowledgements We acknowledge support from the Natural Sciences and Engineering Research Council of Canada and from the U.S. National Science Foundation (NSF) through Grant #1624232 (formerly #1437535). The information presented in this publication is the sole opinion of the authors and does not necessarily reflect the views of the sponsors or sponsoring agencies.

Appendix A. Pseudo code for fragment definition

The following pseudo code outlines the method used to delineate the fragments in the pervasive fragmentation results presented in the paper. The objective of the code is to create a list of fragments and all bulk elements belonging to that fragment.

Algorithm 1 Procedure for determining distribution of fragments.

```
input: nBulkElems          // number of bulk elements in model
  nVisited = 0             // number of bulk elements visited
  while (nVisited < nBulkElems)
    Iterate over all elements in model
      if (element is cohesive) continue; end if
      if (element has been visited) continue; end if
      Create new fragment structure
      Add bulk element to fragment, and flag as visited
      Increment nVisited
      for (i = 0; i < number of bulk elements in fragment; i++)
        Get current element in fragment
        for (j = 0; j < number of adjacent elements; j++)
          if adjacent element is cohesive and not flagged as visited
            Flag cohesive element as visited
            if (cohesive element has failed completely) continue; end if
            for (k = 0; k < number of adjacent bulk elements; k++)
              if (element has been visited) continue; end if
              Add bulk element to fragment, and flag as visited
            end for
          else
            if (element has been visited) continue; end if
            Add bulk element to fragment, and flag as visited
            Increment nVisited
          end if
        end for
      end for
  end while
output: Fragments
```

References

ABAQUS, Version 6.11 Documentation (2011) Dassault Systemes Simulia Corp. Providence, RI, USA

Afferrante L, Ciavarella M, Valenza E (2006) Is Weibull's modulus really a material constant? Example case with interacting collinear cracks. Int J Solids Struct 43:5147–5157

Areias PMA, Belytschko T (2005) Analysis of three-dimensional crack initiation and propagation using the extended finite element method. Int J Numer Methods Eng 63:760–788

Atluri SN, Zhu T (1998) A new meshless local Petrov–Galerkin (MLPG) approach in computational mechanics. Comput Mech 22:117–127

Barenblatt GI (1959) The formation of equilibrium cracks during brittle fracture: general ideas and hypotheses. Axially symmetric cracks. J Appl Math Mech 23:255–265

Bathe K-J (1996) Finite element procedures. Prentice Hall, Upper Saddle River

Bažant ZP, Chen EP (1996) Scaling of structural failure. Technical Report, Sandia National Laboratories

Bažant ZP, Luo W, Chau VT, Bessa MA (2016) Wave dispersion concepts of peridynamics compared to classical nonlocal damage models. J Appl Mech 83:111004-1–111004-4

Becher PF, Sun EY, Plucknett KP, Alexander KB, Hsueh CH, Lin HT, Waters SB, Westmoreland CG (1998) Microstructural design of silicon nitride with improved fracture toughness: I effects of grain shape and size. J Am Ceram Soc 81:2821–2830

Belytschko T, Fleming M (1999) Smoothing, enrichment and contact in the element-free Galerkin method. Comput Struct 71:173–195

Belytschko T, Lu YY, Gu L (1994) Element-free Galerkin methods. Int J Numer Methods Eng 37:229–256

Belytschko T, Gu L, Lu YY (1994) Fracture and crack growth by element free Galerkin methods. Model Simul Mater Sci Eng 2:519–534

Bishop JE (2009) Simulating the pervasive fracture of materials and structures using randomly close packed Voronoi tessellations. Comput Mech 44:455–471

Bishop JE, Strack OE (2011) A statistical method for verifying mesh convergence in Monte Carlo simulations with application to fragmentation. Int J Numer Meth Eng 88(3):279–306

Bishop J, Martinez MJ, Newell P (2016) Simulating fragmentation and fluid-induced fracture in disordered media using random finite-element meshes. Int J Multiscale Comput Eng 14(4):349–366

Brannon R, Wells J, Erik Strack O (2007) Validating theories for brittle damage. Metall Mater Trans A 38:2861–2868

Caballero A, Molinari JF (2010) Finite element simulations of kidney stones fragmentation by direct impact: tool geometry and multiple impacts. Int J Eng Sci 48:253–264

Caballero A, Molinari JF (2011) Optimum energy on the fragmentation of kidney stones by direct impact. Int J Comput-Aided Eng Softw 28:747–764

Cavendish JC, Field DA, Frey WH (1985) An approach to automatic three-dimensional finite element mesh generation. Int J Numer Methods Eng 21:329–347

Celes W, Paulino GH, Espinha R (2005) A compact adjacency-based topological data structure for finite element mesh representation. Int J Numer Methods Eng 64:1529–1556

Danzer R (1992) A general strength distribution function for brittle materials. J Eur Ceram Soc 10:461–472

Delaunay B (1934) Sur la sphère vide. a la mémoire de Georges Voronoï, Bulletin de l'Académie des Sciences de l'URSS. Classe des sciences mathématiques et na 6:793–800

Dugdale DS (1960) Yielding of steel sheets containing slits. J Mech Phys Solids 8:100–104

Espinosa HD, Dwivedi S, Lu H-C (2000) Modeling impact induced delamination of woven fiber reinforced composites with contact/cohesive laws. Comput Methods Appl Mech Eng 183:259–290

Falk ML, Needleman A, Rice JR (2001) A critical evaluation of cohesive zone models of dynamic fracture. J Phys IV 11:43–50

Field DA (1988) Laplacian smoothing and Delaunay triangulations. Commun Appl Numer Methods 4:709–712

Fischer RA, Tippett LHC (1928) Limiting forms of the frequency distribution of the largest and smallest member of a sample. Proc Camb Philos Soc 24:180–190

Fréchet M (1927) Sur la loi de probabilité de l'écart maximum. Annales de la Société de Mathématique 18:93–116

Freudenthal AM (1968) Statistical approach to brittle fracture, Ch. 6. Academic Press, New York, pp 591–616

Geuzaine C, Remacle J-F (2009) Gmsh: a three-dimensional finite element mesh generator with built-in pre- and post-processing facilities. Int J Numer Meth Eng 79:1309–1331

Hashimoto R, Ogawa A, Morimoto T, Yonaiyama M (1996) Spin test of silicon nitride disk. The 74th JSME Annual Meeting 2:441–442

Hinton E, Rock T, Zienkiewicz OC (1976) A note on mass lumping and related processes in the finite element method. Earthq Eng Struct Dyn 4:245–249

Hughes TJR (2000) The finite element method: linear static and dynamic finite element analysis. Dover Publications, New York

Jayatilaka ADS, Trustrum K (1977) Statistical approach to brittle fracture. J Mater Sci 12:1426–1430

Kallinderis Y, Vijayant P (1993) Adaptive refinement-coarsening scheme for three-dimensional unstructured meshes. Am Inst Aeronaut Astronaut J 31:1440–1447

Kim J-H, Paulino GH (2002) Isoparametric graded finite elements for nonhomogeneous isotropic and orthotropic materials. ASME J Appl Mech 69:502–514

Klein PA, Foulk JW, Chen EP, Wimmer SA, Gao H (2000) Physics-based modeling of brittle fracture: cohesive formulations and the application of meshfree methods. Technical report, Sandia National Laboratories

Lancaster P, Salkauskas K (1981) Surfaces generated by moving least squares methods. Math Comput 37:141–158

Levy S (2010) Exploring the physics behind dynamic fragmentation through parallel simulations. Ph.D. thesis, École Polytechnique Fédérale de Lausanne

Liu WK, Jun S, Zhang YF (1995) Reproducing kernel particle methods. Int J Numer Methods Fluids 20:1081–1106

Lo SH (1991) Volume discretization into tetrahedra—II. 3D triangulation by advancing front approach. Comput Struct 39:501–511

Molinari JF, Ortiz M (2002) Three-dimensional adaptive meshing by subdivision and edge-collapse in finite-deformation dynamic-plasticity problems with application to adiabatic shear banding. Int J Numer Methods Eng 53:1101–1126

Mosler J, Ortiz M (2009) An error-estimate-free and remapping-free variational mesh refinement and coarsening method for dissipative solids at finite strains. Int J Numer Methods Eng 77:437–450

Mota A, Knap J, Ortiz M (2006) Three-dimensional fracture and fragmentation of artificial kidney stones. J Phys Conf Ser 46:299–303

Nayroles B, Touzot G, Villon P (1992) Generalizing the finite element moethod: diffuse approximation and diffuse elements. Comput Mech 10:307–318

Newmark NM (1959) A method of computation for structural dynamics. J Eng Mech Div 85(7):67–94

Nguyen VP, Rabczuk T, Bordas S, Duflot M (2008) Meshless methods: review and key computer implementation aspects. Math Comput Simul 79:763–813

Ortiz M, Pandolfi A (1999) Finite-deformation irreversible cohesive elements for three-dimensional crack-propagation analysis. Int J Numer Methods Eng 44:1267–1282

Ostoja-Starzewski M, Wang G (2006) Particle modeling of random crack patterns in epoxy plates. Probab Eng Mech 21:267–275

Park K (2009) Potential-based fracture mechanics using cohesive zone and virtual internal bond modeling. Ph.D. thesis, University of Illinois at Urbana-Champaign

Park K, Paulino GH, Roesler JR (2009) A unified potential-based cohesive model for mixed-mode fracture. J Mech Phys Solids 57:891–908

Park K, Paulino GH, Celes W, Espinha R (2012) Adaptive mesh refinement and coarsening for cohesive zone modeling of dynamic fracture. Int J Numer Methods Eng 92:1–35

Paulino GH, Celes W, Espinha R, Zhang ZJ (2008) A general topology-based framework for adaptive insertion of cohesive elements in finite element meshes. Eng Comput 24:59–78

Paulino GH, Park K, Celes W, Espinha R (2010) Adaptive dynamic cohesive fracture simulations using nodal perturbation and edge-swap operators. Int J Numer Meth Eng 84:1303–1343

Peirce FT (1926) Tensile tests for cotton yarns, part V: the weak wink wheorems on the strength of long and composite specimens. J Text Inst 17:355–368

Pittomvils G, Vandeursen H, Wevers M, Lafaut JP, De Ridder D, De Meester P, Boving R, Baert L (1994) The influence of internal stone structure upon the fracture behavior of urinary calculi. Ultrasound Med Biol 20:803–810

Rabczuk T, Belytschko T (2004) Cracking particles: a simplified meshfree method for arbitrary evolving cracks. Int J Numer Methods Eng 61:2316–2343

Santare MH, Lambros J (2000) Use of graded finite elements to model the behavior of nonhomogeneous materials. J Appl Mech 67:819–822

Schröberl J (1997) Netgen—an advancing front 2D/3D-mesh generator based on abstract rules. Comput Vis Sci 1:41–52

Schroeder WJ, Shephard MS (1988) Geometry-based fully automatic mesh generation and the Delaunay triangulation. Int J Numer Meth Eng 26:2503–2515

Silling SA, Bobaru F (2005) Peridynamic modeling of membranes and fibers. Int J Nonlinear Mech 40:395–409

Simo JC, Wriggers P, Schweizerhof KH, Taylor RL (1986) Finite deformation post-buckling analysis involving inelasticity and contact constraints. Int J Numer Methods Eng 23:779–800

Song JH, Belytschko T (2009) Cracking node method for dynamic fracture with finite elements. Int J Numer Methods Eng 77:360–385

Spring DW, Giraldo-Londono O, Paulino GH (2016) A study on the thermodynamic consistency of the Park-Paulino-Roesler (PPR) cohesive fracture model. Mech Res Commun 78:100–109

Sukumar N, Moes N, Moran B, Belytschko T (2000) Extended finite element method for three-dimensional crack modeling. Int J Numer Methods Eng 48:1549–1570

Sulsky D, Schreyer L (2004) MPM simulation of dynamic material failure with a decohesion constitutive model. Eur J Mech A Solids 23:423–445

Sun EY, Becher PF, Plucknett KP, Hsueh CH, Alexander KB, Waters SB (1998) Microstructural design of silicon nitride with improved fracture toughness: II Effects of yttria and alumina additives. J Am Ceram Soc 81:2831–2840

Swank LR, Williams RM (1981) Correlation of static strengths and speeds of rotational failure of structural ceramics. Am Ceram Soc Bull 60:830–834

Vocialta M, Richart N, Molinari JF (2016) 3D dynmaic fragmentation with parallel dynamic insertion of cohesive elements. Int J Numer Meth Eng 109:1655–1678

von Mises R (1936) La distribution de la plus grande de *n* valeurs. Rev Math Union Interbalcanique 1:141–160

Wang G, Al-Ostaz A, Cheng AH-D, Raju Mantena P (2008) Particle modeling of dynamic fracture simulation of a 2D polymeric material (nylon-6,6) subject to the impact of a rigid indenter. Comput Mater Sci 44:449–463

Weibull W (1939) A statistical theory of the strength of materials. Proc R Acad Eng Sci 151:1–45

Zhang Z (2003) Cohesive zone modeling of dynamic failure in homogeneous and functionally graded materials, Master's thesis, University of Illinois at Urbana-Champaign

Zhang Z, Paulino GH (2005) Cohesive zone modeling of dynamic failure in homogeneous and functionally graded materials. Int J Plast 21:1195–1254

Zhang Z, Paulino GH, Celes W (2007) Extrinsic cohesive zone modeling of dynamic fracture and microbranching instability in brittle materials. Int J Numer Methods Eng 72:893–923

Zhong P, Chuong CJ, Goolsby RD (1992) Microhardness measurements of renal calculi: regional differences and effects of microstructure. J Biomed Mater Res 26:1117–1130

Zhong P, Chuong CJ, Preminger GM (1993) Characterization of fracture thoughness of renal calculi using a microindentation technique. J Mater Sci Lett 12:1460–1462

Zhou F, Molinari JF (2004) Dynamic crack propagation with cohesive elements: a methodology to address mesh dependency. Int J Numer Meth Eng 59:1–24